UNIVERSITY OF OSLO
Department of Physics

Hitchhiking Bistatic Radar

Sindre Strømøy

May 21, 2013

Abstract

A Hitchhiking Bistatic Radar (HBR) consists of a passive receiver *hitch-hiking* on a cooperative or non-cooperative monostatic radar host. The advantages of bistatic radar stems from the separation of the transmitter and receiver which also introduces complexity in synchronization and target location.

An experimental HBR receiver has been developed in collaboration with FFI. The HBR sites, located at Kjeller (receiver) and Kongsvinger (host), was evaluated in the term project [23] and found to be a reasonable location for experimental measurements. Commercial aircrafts are used as targets of opportunity and detections are verified by ADS-B data. Due to the close proximity to Oslo Airport at Gardermoen, targets of opportunity are plentiful.

Link budgets and measurements of the front-end components where made to estimate the detection capabilities. The receiving antenna is mounted on a pan/tilt pedestal directed to point at targets of opportunity to achieve maximum target dwell time, thus mimicking an electronically scanned antenna.

Using real life data, methods for estimation of radar waveform parameters, PRF and scan-time for improved synchronization and localization of targets is demonstrated PRF synchronized Time-Range matrix is used to display raw data along with ADS-B data converted to bistatic range to verify target detections. A large aircraft was detected 100km from the receiver site and an estimated range of 180km for similar targets is proposed.

Pulse compression, non-coherent integration and coherent range-Doppler integration were applied on real life data. Target detections were plotted on a Cartesian grid by solving the geometry for the bistatic triangle.

The HBR receiver could in certain situations improve target detection. In particular modern radars, offering high flexibilty, beam steering and waveform design, could serve as a viable cooperative transmitter.

Contents

1 Introduction **9**
- 1.1 Definitions . . . 9
- 1.2 Thesis objectives . . . 9
- 1.3 Similar research . . . 10

2 Hitchhiking Bistatic Radar Principles **12**
- 2.1 Bistatic Radar . . . 12
  - 2.1.1 Bistatic Geometry . . . 12
  - 2.1.2 Bistatic Range . . . 13
  - 2.1.3 Earth curvature and bistatic line of sight . . . 18
  - 2.1.4 Bistatic Doppler . . . 19
  - 2.1.5 Target Resolution and Location . . . 20
- 2.2 Target Detection . . . 22
- 2.3 Pulse compression with Barker code . . . 24

3 Experimental HBR Receiver Hardware Setup **28**
- 3.1 The superheterodyne receiver . . . 31
  - 3.1.1 Analog Front-End Section . . . 33
  - 3.1.2 Digital back-end section . . . 37
- 3.2 Overall Performance of the HBR Receiver . . . 38
- 3.3 P/T pedestal and ADS-B tracking . . . 40

4 Experimental Measurements **42**
- 4.1 Basic operational properties of transmitter and receiver . . . 42
- 4.2 Set-up Locations . . . 45
- 4.3 Noise measurements . . . 47
- 4.4 Direct Signal Measurements . . . 47
  - 4.4.1 Identifying the direct signal . . . 48
  - 4.4.2 Scan-time measurements for improved target location 49
  - 4.4.3 Phase Measurements for Coherent Processing . . . 50
- 4.5 Target detections . . . 53
  - 4.5.1 Detection verificatian through ADS-B reference . . . 53
  - 4.5.2 Range Estimation . . . 56

5 Digital Signal Processing Techniques **57**
- 5.1 Pulse compression . . . 57
- 5.2 Pulse integration . . . 58
- 5.3 Pulse-Doppler Processing . . . 60
- 5.4 Target Location . . . 64

6 Future Perspectives and System Potential **66**
6.1 Hitchhiking on a non-cooperative host 66
6.2 Hitchhiking on a Cooperative Host 68
6.3 System potentials with enhanced probability of detection . . . 69

7 Summary and Conclusions **72**

A Hardware Descriptions **76**
A.1 Antenna 76
A.2 LNA 76
A.3 RF-BP 76
A.4 Mixer 77
A.5 IF-BP 77
A.6 IF-AMP 78

B Spreadsheets **79**
B.1 Noise Figure Calculator 79
B.2 Bistatic Equation Parameters 82
B.3 Noise Figure Calculator 83
B.4 Target Track 85

C PT-3002 Pelco-D Steering **86**

D Matlab Codes **90**

List of Figures

1 Bistatic triangle in a North-referenced plane. [26, p.60] 13
2 Iso-range contour in the bistatic plane[26, p.77]. 14
3 Bistatic range resolution in the bistatic plane [26, p.78]. . . . 15
4 Ovals of Cassini, contours of constant S/N [26, p.72]. 17
5 Illustrated LOS constrains for targets at altitude h_T 19
6 Bistatic Doppler [26, p.120]. 19
7 Common beam area for target detection with iso-range contours illustrating the range resolution, adapted from[26]. . . . 20
8 The HBR range resolution as a function of $\Delta\theta_T$ [17, p.69]. . . 21
9 PDF of noise amplitude and signal plus noise amplitude[13, p.42]. 23
10 Upper: Barker-13 code. Bottom: Barker modulated sine wave. [23] 25
11 Ambiguity function of Barker-13 generated with the Matlab function - ambfun(). 26
12 Contours of the Barker-13 ambiguity function, generated with the Matlab function - ambfun(). 26
13 Auto-coorelation of the barker modualed signal (blue) and a unmodulated pulse (red). Auto-coorelation in time is the equivialent to the zero Doppler cut of the ambiguity function. [23] 27
14 Receiving antenna mounted on the P/T pedestal. Only one dish is used during experiments. Camera is used for true North referencing and video caption of targets. 29
15 Rack with hardware components. From the top: Front-end receiver, toolbox, NI FlexRIO with FPGA and ADC modules, GPS clock, monitor with keyboard, SBS-1 ADS-B receiver, RF syntheszier, control and storage computer 30
16 Schematics of the basic components of the experimental HBR receiver 31
17 Schematics superhet receiver 32
18 Front-end components 33
19 Radiation pattern for a uniform circular aperture with a diameter of 0.7m operating at a frequency of 1.3GHz 34
20 Down conversion in the frequency domain. The illustration is based on figures in [2, p.165] and [4, p.231] 36
21 Spurious Products up to 6. harmonics[8]. Red square marks the required IF. The required output product is marked with green and the closest spur is marked with red. 37
22 Schematics of FPGA code 38
23 Experimental HBR locations with illustrated half power antenna beam 44

24 Diffraction loss (dB) form T_X (red cross) to R_X (black cross). Adopted from [17]. 46
25 Required target altitude (m) for bistatic LOS [23] 47
26 Noise measurements after pulse compression 48
27 Measurements of the DS as signal power vs. time. The upper plot graph is increasingly zoomed in at the middle and bottom plot. 49
28 Intensity plot over time vs. Bistatic range 50
29 Cut at zero bistatic range of the time-range matrix to illustrate scan time 51
30 Comparing several DS pulses to measure transmitter beamwidth 51
31 Unwrapped phase (rad) of time synchronized DS pulses. The slant slope of the unwrapped phase indicates a consistent offset in frequency. 53
32 Time-range plot with ADS-B plots 54
33 Time-range plot with ADS-B data showing multiple target detections in one scan. (Background of upper right image courtesy of Flightradar24.com) 55
34 Measured S/N of target is in blue and the dotted red line shows relative S/N loss caused only by $R_T^2 R_R^2$ in the bistatic radar equation 56
35 Pulse compression applied on real data, where the red curve is the matched filter response, while the blue curve is the amplitude response of the Barker code. 58
36 Pulse integration effects of the noise 60
37 Range cut from time-range matrix, target marked in red square. 60
38 Time Range 62
39 Linear phase correction 62
40 Target phase over pulses 63
41 Range-Doppler plot with N=16 pulses 63
42 Azimuth-range 64
43 Detections from one scan converted to a transmitter centered Cartesian grid. 65
44 Coverage area for commercial airlines (RCS=$10m^2$) at cruising altitude (adapted from [23]). 67
45 LOS constrained coverage area for low signature targets (RCS=$0.1m^2$) at altitude of 1500m (adapted from [23]). . . . 68
46 Combined coverage area for low signature targets (RCS=$0.01m^2$) within bistatic LOS (adapted from prosjekt). 71
47 Transmitter(!) position moved to illustrate range extension completely outside the host's coverage area. 71
48 RF-BP 1200-1400MHz 77

Nomenclature: Acronyms and Other Abbreviations

ADC	Analog to Digital Converter
ADS-B	Automatic Dependent Surveillance-Broadcast (avionic surveillance technology which include GPS-location broadcasting)
AOA	Angle of Arrival
ATC	Air Traffic Control
BP	Band Pass
COTS	Commercial Of-The-Shelf
DDC	Digital Down Converter
DS	Direct Signal
DSP	Digital Signal Processing
FFI	Norwegian Defence Research Establishment (Forsvarets forskningsinstitutt)
FPGA	Field-Programmable Gate Array
GPS	Global Positioning System
HBR	Hitchhiking Bistatic Radar
HDD	Hard Disk Drive
HPBW	Half Power Bandwidth
I/Q	In-Phase/Quadrature
IF	Intermediate Frequency
I.L	Insertion Loss
LNA	Low Noise Amplifier
LO	Local Oscillato
LOS	Line Of Sight
NI	National Instruments
P/T	Pan/Tilt
PDF	Probability Distribution Function
PPI	Plan Position Indicator
PRF	Pulse Repetion Frequency
PRI	Pulse Repetion Interval
RCS	Radar Cross Section
RF	Radio Frequency
S/N	Signal-to-Noise ratio
DS	Direct Signal
RMS	Root Mean Square
UCL	University College London
VSWR	Voltage Standing Wave Ratio

List of symbols

A_R	receiver-target azimuth angle
A_{RT}	receiver-transmitter azimuth angle
A_T	transmitter-target azimuth angle
B	bandwidth
B_n	noise bandwidth of receiver's prediction filter
c	speed of light
E_R	receiver-target elevation angle
E_T	transmitter-target elevation angle
E_{RT}	receiver-transmitter elevation angle
f_{DB}	bistatic doppler shift
F_T	pattern propagation factor for transmitter-to-target path
F_R	pattern propagation factor for receiver-to-target path
G_T	transmitting antenna power gain
G_R	receiving antenna power gain
k	Boltzmann's constant
T_X	transmitter location
R_X	receiver location
T	target location
L	transmitter to receiver baseline range
R_R	target to receiver range
R_T	transmitter to target range
β	bistatic angle
θ_R	receiver look angle
θ_T	transmitter look angle
δ	target velocity vector angle
ΔR_B	bistatic range resolution
$(R_T + R_R)$	bistatic range sum
$(...)_{maxunamb}$	maximum unambiguous of ...
Δt_{tt}	time from pulse leaving trasmitter until target echo reaches the receiver
Δt_{tr}	time from direct signal reveived until target echo received
(S/N)	signal-to-noise ratio
$(S/N)_{min}$	minimum signal-to-noise ratio required for detection
P_T	transmitter power output
λ	carrier frequency wavelength
σ_B	bistatic radar target cross section
T_S	receiving system noise temperature
L_T	transmitting system losses (> 1) not included in other parameters

L_R	receiving system losses (> 1) not included in other parameters
$\dot{R}_T + \dot{R}_R$	combined bistatic range rate
v	velocity
δ	angle between target velocity vector and /2
f_c	carrier frequency
f_{image}	image frequency
f_{LO}	local oscillator frequency
f_{IF}	intermediate frequency
η	antenna efficency
h_T	transmitter altitude
h_t	target altitude
h_R	receiver altitude
χ	time-range matrix

1 Introduction

In the beginning of the 20th century, the very first radar systems were bistatic as the duplexer needed for a collocated transmitter and receiver was yet to be invented. However, since the inventions of the duplexer allowing pulsed waveforms to be transmitted with the same antenna, the monostatic radar has been the preferred choice as the primary radar in air surveillance. With potential threats becoming faster, more agile and stealthier [3], a hitchhiking bistatic radar (HBR) may serve as a low cost addition to improve sensitivity and coverage of existing monostatic radars in order to cope with these new threats.

1.1 Definitions

A bistatic radar is defined in IEEE Standard Radar Definitions [1] as

> *A radar using antennas for transmission and reception at sufficiently different locations that the angles or ranges to the target are significantly different.*

A Hitchhiking Bistatic Radar (HBR) consists of a passive receiver *hitchhiking* on a cooperative or non-cooperative monostatic radar host. Although the term hitchhiking has been used to describe different types of bistatic operations, this term will here only be used to describe operations where the transmitter of opportunity is a stand-alone monostatic radar, as defined by Willis[26]. The HBR acronym is used throughout this thesis for convenience. It is intended to serve as a distinction between HBR and the more common Passive Bistatic Radar (PBR) [1] which is mainly used to describe Passive Coherent Location (PCL) operations where radio or television broadcasters is used as transmitters of opportunity [27], although HBR is a subset of PBR.

1.2 Thesis objectives

The basis of this thesis was formed during a summer internship at FFI, where a system to point an antenna at an ADS-B reporting target was developed. The antenna and concept points in the direction of an electronically scanned/steered antenna, and will be mimicked by using this directed antenna. The next step was taken during a term project where theoretical calculations based on bistatic radar theory were used to estimate the coverage area of a HBR located at FFI. With the use of hardware developed at FFI, this thesis objectives are

- Finish building the RF Front-End of an HBR receiver to provide for a functional sensor system with continuous sampling of measurements
- Verify the theoretical calculations from the term project by measurements

- Implement bistatic processing techniques to improve system performance, including pulse compression and non-coherent integration
- If possible, develop and test techniques for target localization
- Discuss possibilities and limitations for HBR systems as a complemetary air surveillance sensor

All topics have been answered to, and in addition the signal processing has been taken one step further by estimating radar waveform parameters and thus exploiting coherent processing.
The outline and contents of the thesis may be summarized as:

Chapter 2 presents the basic theory about the geometrical properties of the bistatic radar, pulse compression and basics common to most radar systems.

Chapter 3 describe the hardware of the experimental sensor system and the considerations that was taken in the choice of the Front-End components.

Chapter 4 describes the geographic location of the HBR experiment and presents measurement results.

Chapter 5 demonstrates bistatic radar processing techniques on real data from the experimental sensor system, including pulse compression, non-coherent integration, pulse-Doppler processing and target localization

In chapter 6 some possible HBR applications for air surveillance are discussed.

Chapter 7 summaries the previous chapters for a conclusion and suggestions for further work are given.

The remainder of this chapter will focus on open literature research.

1.3 Similar research

The nature of a hidden, low cost, as well as potential stealth countermeasures radar system has made the open literature research on bistatic radars rather limited. However, after searching through IEEE Explore and Google for HBR related research, the following research is considered related:

The first operational HBR, the German Klein Heindelberg [6] was already in use during the Second World War. Since then, Bistatic radar has had three resurgences, with the third and current being mostly dominated by PBR [27]. However, these resurgences have not resulted in many bistatic radars operational today. To quote Professor Hugh Griffiths [7] from an article from 2003

> *Over the years a number of bistatic radar systems have been built and evaluated. However, rather few have progressed beyond the 'technology demonstrator' phase.*

The only successful military application of bistatic radar is the semi-active homing missile system concept, while it might be argued that the PCL-technology is also being promising, such as the Lockheed Martin's Silent Sentry systems and the Thales Home Alerter 100 [27].

As part of *Argus 3D*, a recently ended project (January 2013) funded by the European Commission, a study of simulations with a network of HBR where conducted by Bumar Elektronika (Poland). They concluded that a network of HBR receiver can extend the range of a ATC radar and will improve localization with a hyperbolic positioning method when target is detected by three or more receivers [16].

A short summary of each of the three experiments is given below, where the baseline is defined as the distance between the host and the experimental receiver and f_c is the carrier frequency of the radar:

An article from 1982 by J. G. Schoenenberger and J. R. Forrest at UCL [20] describe an experimental HBR hitchhiking on an Air Traffic Control (ATC) radar at London Heathrow airport (f_c=600Mhz) with a baseline distance of 25km. The synchronization was made during the direct signal dwell time of 25 pulses and a real-time Plan Position Indicator (PPI) was developed, capable of detecting targets up to 75km away and tracked as far as 130km.

An experiment named *BRENDA* is described in an article from 1993 [5]. A monopole antenna and a dedicated directional antenna for synchronization was used to Hitchhike on an ATC radar at Barcelona airport (f_c=2.7 GHz and staggered PRF), with a baseline of 11km. No target detection is mentioned, only ground clutter.

HBR experiments conducted at FFI is referenced in three articles from 2005-2007 [12][19][24]. A receiving monopole antenna was used to hitchhike on a ATC radar (fc=1.3 GHz), at Lørenskog, Norway with a baseline of 10km. A continuously updated clutter map and "target back propagation" was used for clutter suppression and a real time digital display with target trace was developed.

The experimental work in this thesis differs from the listed experiments with an extended baseline of about 60km and where the host is not in LOS. In addition, other digital signal processing techniques, such as pulse compression, non-coherent integration and coherent Doppler processing is evaluated.

2 Hitchhiking Bistatic Radar Principles

What does a hitchhiking bistatic radar (HBR) measure, how does it measure it and what needs to be calculated or processed in order to detect and locate targets? This chapter presents the theoretical background on which this thesis is based on. Theory involving the hardware implementations is, as mentioned in the introduction, included in chapter 3 and therefore not contained in this chapter. The theoretical background includes the special geometrical properties of the bistatic radar and basics common to most radar systems. Parts of this theory was described in a term project [23] and is modified here with additional new aspects that includes; LOS constrains, bistatic RCS, Doppler resolution, target resolution, target detection and the ambiguity function. The bistatic geometry has been described in detail by Jackson[11] and bistatic radar in whole has been thoroughly described by Willis in "Bistatic Radar"[26]. The notation in the latter is adopted throughout this work.

2.1 Bistatic Radar

Bistatic radar is a class of radar system. The term *bistatic* refers to the spatially separated locations of the transmitter (T_X) and receiver (R_X) of these radar systems. The term is used to distinguish a bistatic radar from radar systems of a monostatic type, were R_X and T_X are colocated, which is generally referred to as just radar. The distance between R_X and T_X in a bistatic radar, known as the *Baseline* (typically denoted as L), needs to be comparable to the target range (R_R) in order to provide the advantages of the bistatic geometry. Two common methods of measuring range with HBR will be discussed; synchronization with the time the transmitter emits the signal and synchronization with the time the direct signal from the transmitter reaches the receiver. When dealing with bistatic radar, this simple observation, introduced by Willis[26, p.], is useful as a "sanity check":

> *In all cases bistatic operations collapses to monostatic operation by setting* $L = 0$ *or* $R_T = R_R$ *and* $\beta = 0°$ *in bistatic equations.*

2.1.1 Bistatic Geometry

The main parameters in bistatic radar, namely the transmitter (T_X), the receiver (R_X) and the target (T), makes up the bistatic triangle. Figure 1 shows the bistatic triangle and its geometrical relations in a North-referenced plane. Conversions from the receivers angle of arrival (AOA) measurements from true North-referenced spherical coordinates to the look angle (θ_R) on the bistatic plane is described in section 2.1.5.

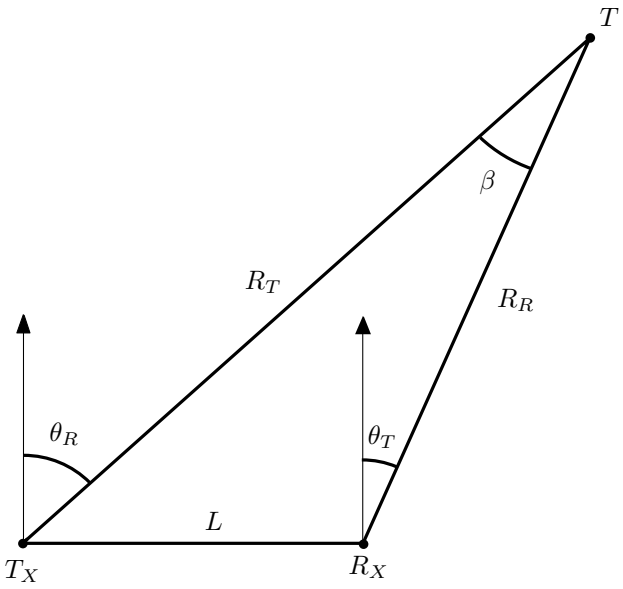

Figure 1: Bistatic triangle in a North-referenced plane. [26, p.60]

2.1.2 Bistatic Range

A HBR measures the time a signal has traveled from T_X to R_X. When scattered off a target, the combined distance travel by the signal equals to the range sum of $R_T + R_R$.

$$(R_T + R_R) = c\Delta t_{tt} \tag{1}$$

Where Δt_{tt} is the time taken from the transmission from T_X until the target echo reches the receiver. If synchronizing with the time the direct signal from the transmitter reaches the receiver, the range sum can be calculated as

$$(R_T + R_R) = c\Delta t_{rt} + L \tag{2}$$

where L is the baseline distance from T_X to R_X and Δt_{rt} is the time in between the direct signal and the target echo. Having no information about the direction of the target, i.e with omnidirectional antennas, the location of the target will be anywhere on the iso-range contour which forms an ellipsoid with Rx and Tx as foci. In the bistatic plane in which the bistatic triangle lies in, an iso-range contour forms an ellipse. The bistatic iso-range in a plane, with the transmitter and receiver locations, is shown in Figure 2.

The range resolution is given by the bandwidth (B) of the transmitted pulse and the bistatic angle of the target location. The range resolution is

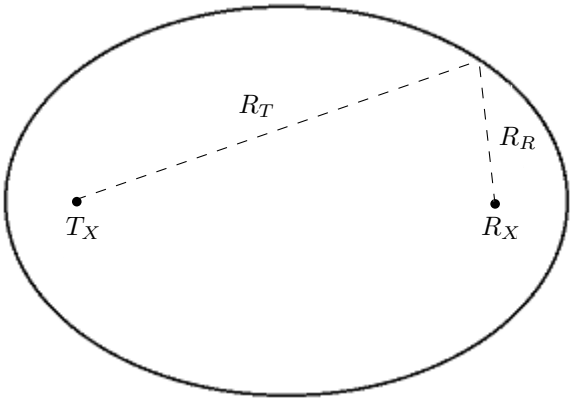

Figure 2: Iso-range contour in the bistatic plane[26, p.77].

defined as the distance between two iso-range contours separated by a time equal to the inverse of the pulse bandwidth. The differences of the width of the range cell is illustrated in Figure 3. An exact, but implicit, expression of the bistatic range resolution is given in the appendix in "Bistatic Radar"[26]. In a more general form, the width of the bistatic range cell [11] can be approximated by

$$\Delta R_B \approx \frac{c}{2B\cos(\beta/2)} \tag{3}$$

where c, the speed of light in vacuum, is used as an approximation instead of the true propagation speed which in air is slightly less than c (with a range of 100km in normal atmosphere gives an error of about 30m when using c). Compared with the range resolution of the monostatic transmitter, the width of the bistatic range cell is always greater or equal (when $= 0$) to the width of the monostatic range cell, which is

$$\Delta R_M = \frac{c}{2B} \tag{4}$$

The range at which a HBR can locate a target is either constrained by

- the maximum unambiguous range caused by the pulse repetition frequency (PRF) of the host.
- the thermal noise, where the target echo cannot by separated from the thermal noise seen in the receiver.
- the Line-of-sight (LOS), where the target is out of the LOS of either the transmitting or receiving beam.

The maximum unambiguous range in a pulsed HBR is given by the distance a target echo can reach the receiver before the next pulse is emitted.

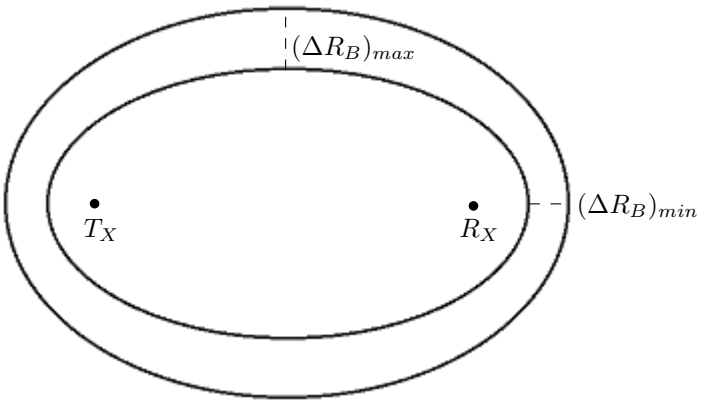

Figure 3: Bistatic range resolution in the bistatic plane [26, p.78].

When hitchhiking on pulsed radar with constant PRF, the maximum unambiguous range can limit the operating region of the HBR. Since the electromagnetic signals are travelling close to the speed of light (c), the maximum unambiguous range of a bistatic radar becomes[26, p.115]

$$(R_R + R_T)_{maxunamb} = \frac{c}{PRF} \tag{5}$$

The maximum range of the HBR can therefore be limited by the host's PRF. When hitchhiking on long range air surveillance/defense radars, the PRF is usually low enough to not inflict on the operating region of the HBR. Low PRF will however give ambiguous measurements of the targets velocity, as described in section 2.1.4.
A target's *visibility* is dependent on whether the target is detectable, that is if the signal from the target echo is strong enough to be separated from the noise seen in the receiver. The maximum range a target is visible is given by the range equation. The bistatic range equation can by derived in a completely analogous matter to that for a monostatic radar [26, p.67-68] and can be written as

$$(R_T R_R)_{max} = \sqrt{\frac{P_T G_T G_R \lambda^2 \sigma_B F_T^2 F_R^2}{(4\pi)^3 k T_s B_n (S/N)_{min} L_T L_R}} \tag{6}$$

R_R	target to receiver range
R_T	transmitter to target range
P_T	transmitter power output
G_T	transmitting antenna power gain
G_R	receiving antenna power gain
λ	carrier frequency wavelength
σ_B	bistatic radar target cross section
F_T	pattern propagation factor for transmitter-to-target path
F_R	pattern propagation factor for receiver-to-target path
k	Boltzmann's constant
T_S	receiving system noise temperature
B_n	noise bandwidth of receiver's prediction filter
$(S/N)_{min}$	minimum signal-to-noise ratio required for detection
L_T	transmitting system losses (> 1) not included in other parameters
L_R	receiving system losses (> 1) not included in other parameters

Table 3: Bistatic range equation parameters

The radar cross section (RCS) of the target (σ_B) is subscripted with a B for bistatic, since it usually differs from the monostatic RCS except when the bistatic angle is close to zero. The difference between monostatic and bistatic RCS is not only depend on the aspect angle and bistatic angle, but also the physical characteristics of the target, such as size relative to the wavelength, shape and surface. Willis [26, p.145-155] separates the bistatic RCS in three regions: the pseudo-monostatic, bistatic and forward-scatter region defined by the bistatic angle, and the extent of these regions are defined by physical characteristics of the target. In short, the bistatic RCS is similar to the monostatic RCS in pseudo-monostatic region, either less or greater in the bistatic region depending on the shape of the target and usually greater in the forward-scatter region, at least for low signature targets, due to the Babinet's principle [26, p.218] where the forward-scattered RCS is given as

$$\sigma_F = \frac{4\pi A^2}{\lambda^2} \tag{7}$$

where A is the physical area of the cross section.

The propagation factors F_T and F_R describes the effects from the natural environment along the path of the signal, which includes diffraction, multipath and refraction [21]. The propagation factors are separated for the two bistatic paths, R_T and R_R, as the propagation effects along these paths can be significantly different. This separation is useful when comparing the HBR and the monostatic host as seen in section 6.3. L_T and L_R includes the losses from respectively transmitter-target and target-receiver which is

not included in the propagation factor or in the system noise temperature (T_s).
The range equations describes the maximum range given by the detection threshold of required signal-to-noise ratio ($(S/N)_{min}$). Modifying the range equation (equation 6) to describe S/N as a function of the bistatic range product ($R_T^2 R_R^2$) gives the bistatic radar equation. The bistatic radar equation solving for S/N [26, p.70] is

$$S/N = \frac{P_T G_T G_R \lambda^2 \sigma_B F_T^2 F_R^2}{(4\pi)^3 R_T^2 R_R^2 k T_s B_n L_T L_R} \tag{8}$$

The bistatic radar equation applies for all types of waveforms. A more specific formulation of this equation might be useful to incorporate the specific signal processing techniques used to improve the S/N. Contours of constant S/N forms ovals of Cassini [26, p.70]. Figure 4 shows the contours of constant S/N as ovals of Cassini, where the baseline is L=50km and the *lemniscate* oval (of two parts) occurring at $S/N = 40dB$. This is where the oval breaks into two parts at the point on the baseline called the *cusp*.

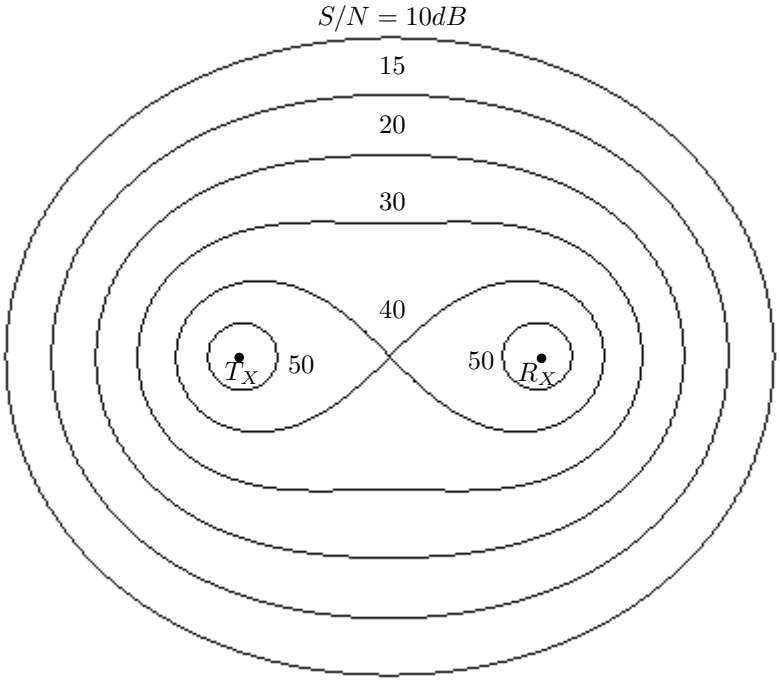

Figure 4: Ovals of Cassini, contours of constant S/N [26, p.72].

The S/N is strongest near the transmitter and receiver site. This is reasonable as the path loss caused by the range product of R_T^2 and R_R^2, is small when either R_T or R_R becomes significantly short. These equations are valid in the far-field of the antennas and $R_T, R_R > 1$. The ovals of Cassini define

three operating regions of a HBR: the receiver centered, the transmitter centered and the co-site region. When HBR is used for air surveillance/defense, the receiver centered region defines short ranged operations, while co-site region involving both receiver and transmitter site defines medium to long range operations.
An equivalent radar equation for the monostatic host can be obtained by setting $G_R = G_T$, $\sigma_M = \sigma_B$, $F_R = F_T$, $R_R = R_T$ and $L_T L_R = L_M$. The monostatic radar equation is then given as

$$(S/N)_M = \frac{P_T {G_T}^2 \lambda^2 \sigma_M F_T^4}{(4\pi)^3 R_T^4 k T_s B_n L_M} \tag{9}$$

and is useful as comparison when estimating the HBR receivers ability to improve coverage of the host. The contours of constant monostatic S/N are spherical or circular in a plane.

2.1.3 Earth curvature and bistatic line of sight

For detection, the target must be simultaneously illuminated by both the transmitter and receiver beam. With this follows the LOS constrains from both the transmitter and receiver sites. Using 4/3 earth model, which is to multiply the earth radius by 4/3 to allow for microwave refraction, the radar horizon can be approximated as a straight line. The 4/3 earth model is commonly used in telecommunications, but should only be used as a guide since the weather can have substantial effects on the actual propagation [11].Given this propagation model, the two-dimensional LOS coverage from the transmitter and receiver site [26, p.108] will then have a radius that can be approximated as

$$r_R = 130(\sqrt{h_t} + \sqrt{h_R}) \tag{10}$$

$$r_T = 130(\sqrt{h_t} + \sqrt{h_T}) \tag{11}$$

where h_t, h_R and h_T is the altitude in km for respectively the target, receiving and transmitting antenna. Figure 5 illustrates the LOS-constrained coverage areas for targets at altitude h_t. If the HBR is synchronized with the direct signal from transmitter, then L must be less or equal to $r_T + r_R$. Thus,

$$L \leq 130(\sqrt{h_R} + \sqrt{h_T}) \tag{12}$$

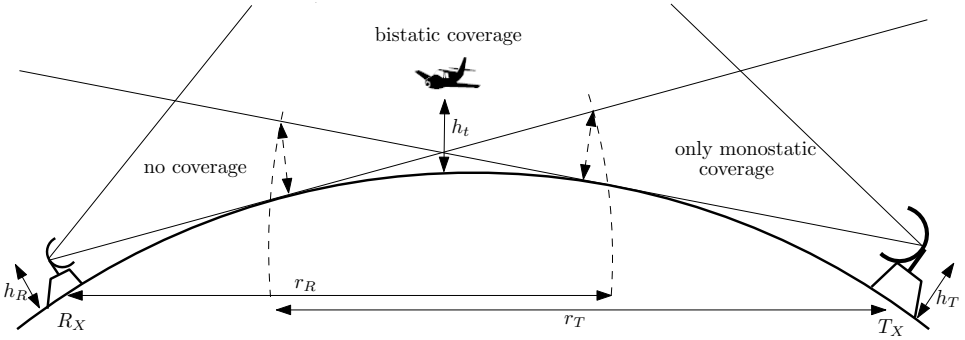

Figure 5: Illustrated LOS constrains for targets at altitude h_T

2.1.4 Bistatic Doppler

The bistatic Doppler shift is the result of the combined range rate of R_T and R_R. From the geometrical relations described by the bistatic triangle and the targets velocity vector, shown in figure 6, the bistatic Doppler shift can be approximated as [26, p.120].

$$f_{D_B} = \frac{\dot{R}_T + \dot{R}_R}{\lambda} = \frac{2v}{\lambda}\cos(\delta)\cos(\beta/2) \tag{13}$$

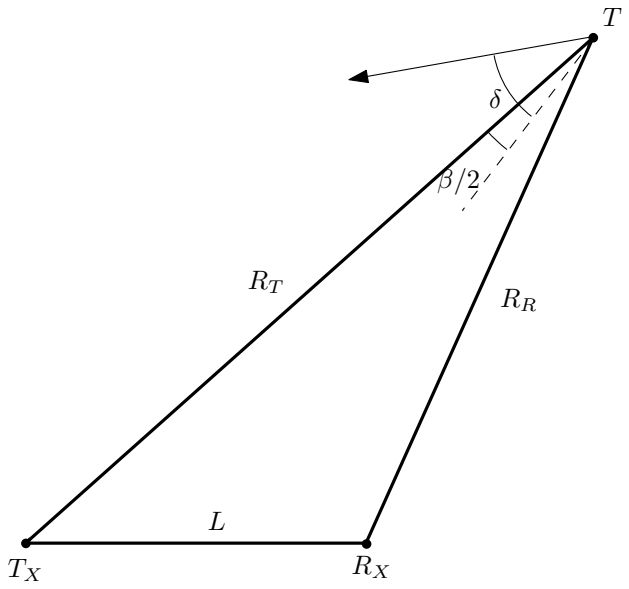

Figure 6: Bistatic Doppler [26, p.120].

Ambiguities in target velocity measures will occur if the Doppler shift caused by the combined range rate exceeds the PRF of the host. Maximum unambiguous Doppler shift is given by

$$(f_{D_B})_{maxunamb} = \pm\frac{PRF}{2} \tag{14}$$

As long as the Doppler shift seen in the receiver is not an exact multiple of the transmitters PRF, it can be used to separate a moving target from stationary clutter. The heading and velocity of the target can be estimated with target locations over several scans. The Doppler resolution is given by the coherent integration time T [26, p.134] as

$$\Delta f_{D_B} = \frac{1}{T} \tag{15}$$

2.1.5 Target Resolution and Location

Target detections are confined to the instantaneously shared volume of the transmitting and receiving beam. Figure 7 shows the two-dimensional area confined by the half power beam width (HPBW) of transmitter ($\Delta\theta_T$) and receiver ($\Delta\theta_R$). The transmitter beam width is deliberately illustrated as smaller then $\Delta\theta_R$ as this is the case with the experimental HBR described in chapter 3.

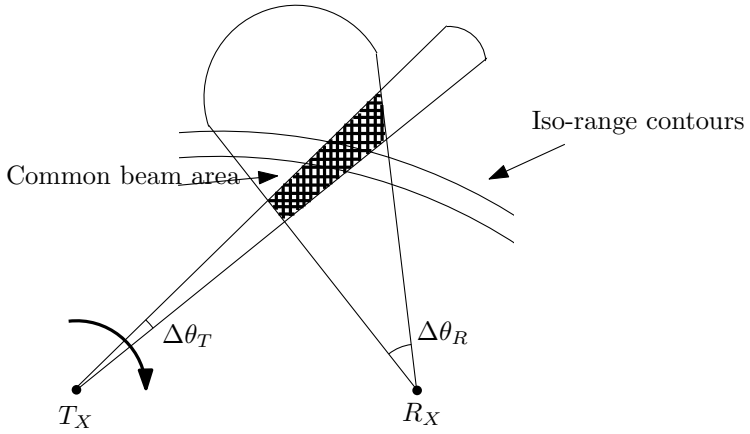

Figure 7: Common beam area for target detection with iso-range contours illustrating the range resolution, adapted from[26].

The angular resolution for a monostatic is usually taken as the HPBW of the antenna ($\Delta\theta_T$). While the monostatic radar resolution is determined only by the transmitted bandwidth B (equation 4) and the angular resolution $\Delta\theta_T$, the bistatic radar resolution becomes more complex due to the bistatic geometry. This is illustrated in figure 8 from [17, p.69], which shows the bistatic radar resolution for an omni-directional antenna and a directional

antenna with $\Delta\theta_T = 10$ degrees and $B = 100$ kHz. We see that the bistatic range and angular resolution is also affected by the geometrical relations.

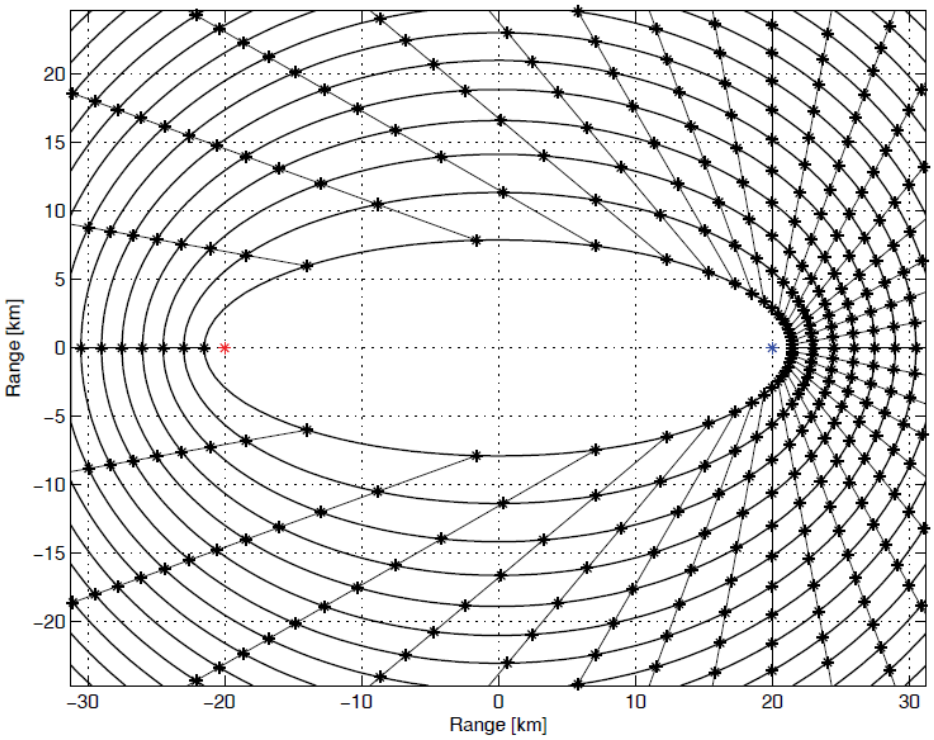

Figure 8: The HBR range resolution as a function of $\Delta\theta_T$ [17, p.69].

Since the monostatic beam contributes on a two-way path, the rejection on the sides becomes 6dB. To achieve the same rejection in a HBR, in the cases were only the one-way path transmitting beam is contributing to the angular resolution, the bistatic angular resolution becomes $2\Delta\theta_T$. Willis propose that the minimum separation of to targets on the same iso-range contour [26, p.135] is then given as

$$(\Delta R_\theta)_u \approx \frac{2\Delta\theta_T R_T}{\cos(\beta/2)} \tag{16}$$

Where u denotes the unequal arc-lengths of the transmitting and receiving beam and where $\theta_T R_T$ is the arc-length of the transmitting beam.

While the range sum (R_T+R_R) or the bistatic range (R_T+R_R-L) is measured, the target position, from either the receiving site or the transmitting site, cannot be measured directly by a HBR receiver. It can however be calculated if the baseline L and receiver look angle θ_R or the transmitter look angle θ_T is known. As the transmitter in a HBR often has a smaller beamwitdh

than the receiver, positions calculation with θ_T will provide higher accuracy. θ_T can be obtained either from a cooperative transmitter or by measurements of the transmitter scan rate. A solution to calculate R_R and R_T is given by solving for the bistatic triangle [26, p.86] (figure 1) as

$$R_R = \frac{(R_T + R_R)^2 - L^2}{2(R_T + R_R + L\sin(\theta_R))} \tag{17}$$

$$R_T = \frac{(R_T + R_R)^2 - L^2}{2(R_T + R_R - L\sin(\theta_T))} \tag{18}$$

Target detections along the baseline cannot be located as the scattered signals from these targets will reach the receiver simultaneously with the direct signal from the transmitter. However, targets can still be detected, as a large forward scatter RCS (σ_F) results in a change in direct signal power seen by the receiver.
The experimental HBR (described in chapter 3 and 4) measures targets AOA from a true North-referenced local coordinate system, as is the target AOA seen from the transmitter measured by the receiver from the transmitter antenna scan rate. For use in the equations17 and 18, conversions to the look angle (θ_R) on the bistatic plane is given as[26, p.103]

$$\theta_R = -\arcsin[\cos(E_R)\cos(E_{RT})\cos(A_R - A_{RT}) + \sin(E_R)\sin(E_{RT})] \tag{19}$$

where A_R and E_R are the receivers true-North azimuth and elevation AOA of target and A_{RT} and E_{RT} is thereceivers true-North azimuth and elevation AOA for of transmitting site. When no elevation information is available or for small grazing angle approximation, equation 19 can be simplified as

$$\theta_R = -\arcsin(cos(A_R - A_{RT})) \tag{20}$$

$$\theta_T = -\arcsin(cos(A_T - A_{RT})) \tag{21}$$

2.2 Target Detection

In order to properly estimate the HBR coverage area, a realistic $(S/N)_{min}$ in equation 6 needs to be selected. An amplitude threshold V_T should be selected to provide a high probability of detection P_D as well as a very low probability of false alarm P_{FA}. P_{FA} is the probability of noise passes the threshold and therefore mistaken as a target. For single pulse detection of targets with constant RCS, Levanon [13, p.39-43] shows that the probability distribution function (PDF) for the envelope of a constant signal with white Gaussian noise passed through the receiver band pass filter becomes a *Rician* PDF. At the extremities, the Rician PDF collapses to a Rayleigh PDF when no signal is present and to a Gaussian PDF for large S/N signals. These PDF can be mathematically expressed as

$$\text{Rician PDF: } p(r) = \frac{r}{\sigma^2} e^{\frac{-(r^2+A^2)}{2\sigma^2}} I_0(\frac{rA}{\sigma^2}) \tag{22}$$

where r is the received amplitude , σ is the standard deviation and A is the amplitude of the signal to be detected. When $A = 0$, the Rician PDF collapess to the Rayleigh PDF

$$\text{Rayleigh PDF: } p(r) = \frac{r}{\sigma^2} e^{\frac{-r^2}{2\sigma^2}} \tag{23}$$

when $A >> \sigma^2$ the Rician PDF can be expressed as the Gaussian (or the normal) PDF

$$\text{Gaussian PDF: } p(r) = \frac{1}{\sigma\sqrt{2\pi}} e^{-\frac{(r-A)^2}{2\sigma^2}} \tag{24}$$

Figure 9 shows the relations between the target threshold V_T, P_D and P_{FA}. Normally the V_T is set much higher than illustrated in figure 9 to achieve a much smaller P_{FA}, typically $P_{FA} < 10^{-6}$.

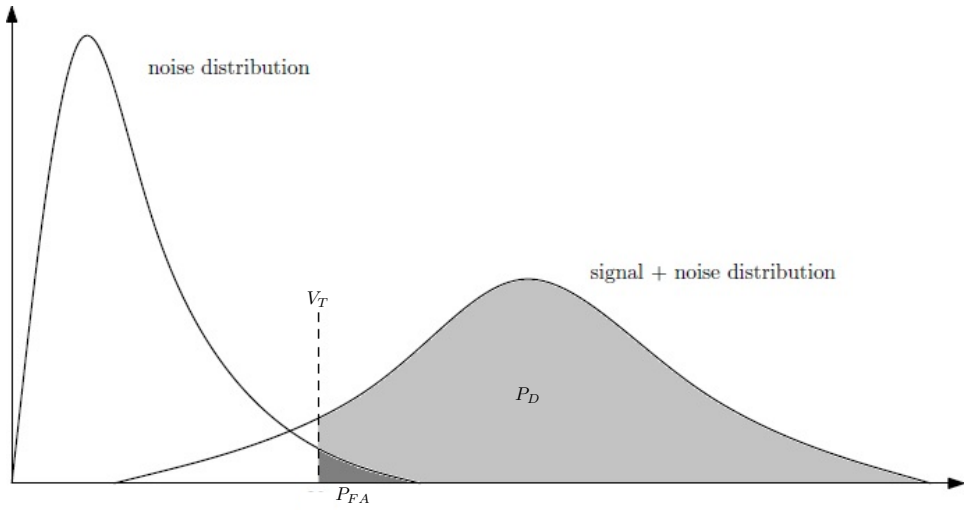

Figure 9: PDF of noise amplitude and signal plus noise amplitude[13, p.42].

The relations between the requierd S/N and the propabilities P_D and P_{FA} can be approximated with this expression[13, p.43]

$$(S/N) = 10\log_{10}(A + 0.12AB + 1.7B) \tag{25}$$

where

$$A = \ln\frac{0.62}{P_{FA}}, B = \ln\frac{P_D}{1-P_D} \tag{26}$$

Equation 25 is fairly accurate when $10^{-7} < P_{FA} < 10^{-3}$ and $0.1 < P_D < 0.9$. Using equation 25 a requirement of $P_{FA} = 10^{-6}$ and $P_D = 0.9$ would result

in a required S/N of about 13dB.
The threshold applies for one pulse signal detection in white noise where the amplitude of the signal is constant. Looking at several pulses before detection by with non-coherent pulse integration will reduce the standard deviations, thus improving P_D , reducing P_{FA} or allows for a reduced threshold V_T. Pulse integration of real data is demonstrated in chapter 5. The threshold also assume constant amplitude signal. However, real-life target has a complex RCS, consisting of multiple reflecting areas contributing to received signal and may also fluctuate from pulse to pulse. Signal distributions of real target scatter is more accurately described with one of the Swirling cases [13]. Also, detection does not distinguish between clutter and target signals so adequate clutter suppression is required in a practical system.

2.3 Pulse compression with Barker code

Pulse compression obtain by Barker coded pulses is described in the term project [23] and is briefly reproduced here in addition to the ambiguity function for monostatic and bistatic radar, which can be used to analyze pulse compression responses. Pulse compression is applied on real data from the experiment and the effects are illustrated in section 5.1.
Pulse compression is obtained by correlating the received signal with the modulated transmitted signal to improve range resolution and S/N. This is achieved by match filtering in a radar, which is the optimal filter for signal detection in white noise. A match filter is described by filtering input signal with a complex conjugated and time-reversed version of the transmitted pulse and can mathematically be expressed as the time convolution of the input signal $s(t)$ and the matched filter impulse response $h(t)$[13][23]

$$(s * h)(t) = K \int_{-\infty}^{\infty} s(\tau) s^*(\tau_d - (t\_t_M)) d\tau \tag{27}$$

where $h(t) = Ks^*(t_M - t)$, s^* denotes the complex conjugate of $s(t)$, K is an amplitude constant, t is time, t_M is observation time and τ is the delay or lag.
Barker coding is used to phase modulate the transmitted pulse signal in order to achieve pulse compression. The Barker code shifts the phase of the signal either by 0 or 180 degrees, which allows for simple realization as the barker coefficients are binary (only two states) and real (as in non-complex). The transmitter in the HBR experiment utilize Barker-13 code which is illustrated in figure **??**. The barker-13 code provides a pulse compression gain (PCG) of about 10dB and a side lobe reduction of about 20dB ($20\log_{10}(13)$). The PCG is defined as the S/N improvement and can therefore be inserted directly in the bistatic radar equation (equation 8).

The displacement in range and Doppler frequency of a point target in additive Gaussian noise can be described by the squared magnitude of the

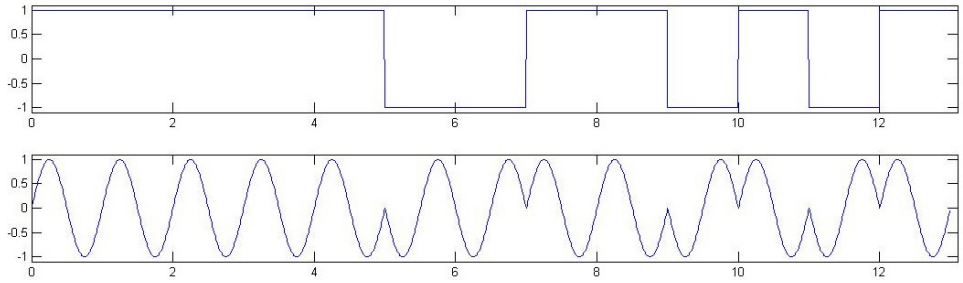

Figure 10: Upper: Barker-13 code. Bottom: Barker modulated sine wave. [23]

ambiguity function ($\chi(\tau, f_D)$) [1], which is mathematically expressed as

$$|\chi(\tau, f_D)|^2 = \left| \int_{-\infty}^{\infty} s(t) s^*(t+\tau) e^{2\pi j f_D t} dt \right|^2 \tag{28}$$

where $\chi(\tau, f_D)$ describes the response at time delay τ and Doppler frequency f_D, and $s(t)$ is the radar waveform (normalized). The ambiguity function can be used to examine radar waveforms in terms of resolution and ambiguities. Figures 11 and 12 shows the ambiguity function of the Barker-13 modulated waveform used by the experimental HBR. Figure 13 illustrates the range ambiguities at zero Doppler frequency[23].

The ambiguity function in equation 28 presumes a monostatic radar. To analyze the ambiguities from the geometrical relations of a specific bistatic radar scene, a bistatic ambiguity function is proposed in [25]. In this thesis, the bistatic ambiguity function spesific to the bistatic target location and heading is not considered and only the transmitted waveform is analyzed.

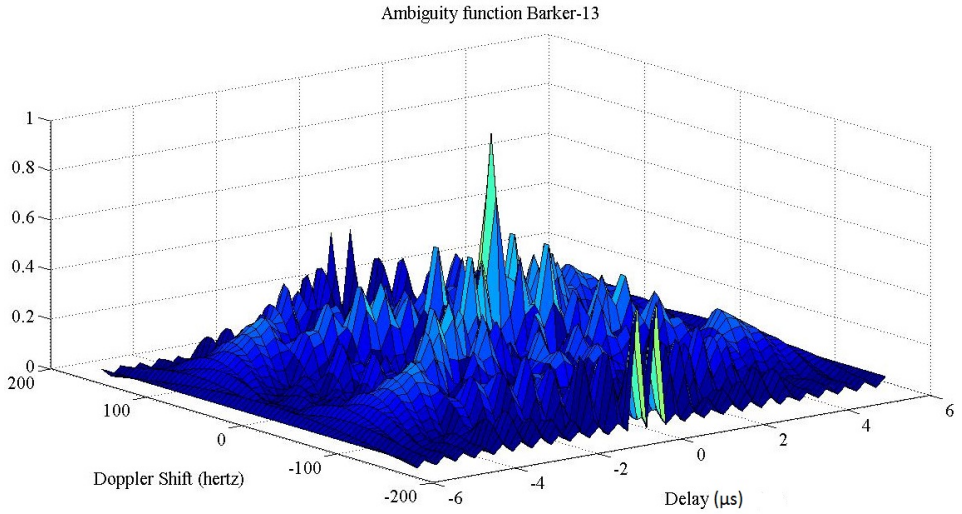

Figure 11: Ambiguity function of Barker-13 generated with the Matlab function - ambfun().

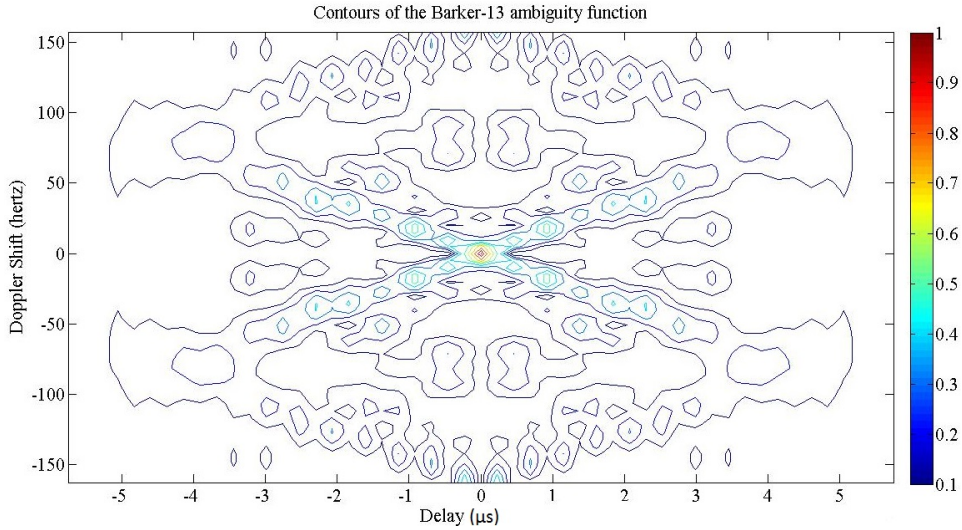

Figure 12: Contours of the Barker-13 ambiguity function, generated with the Matlab function - ambfun().

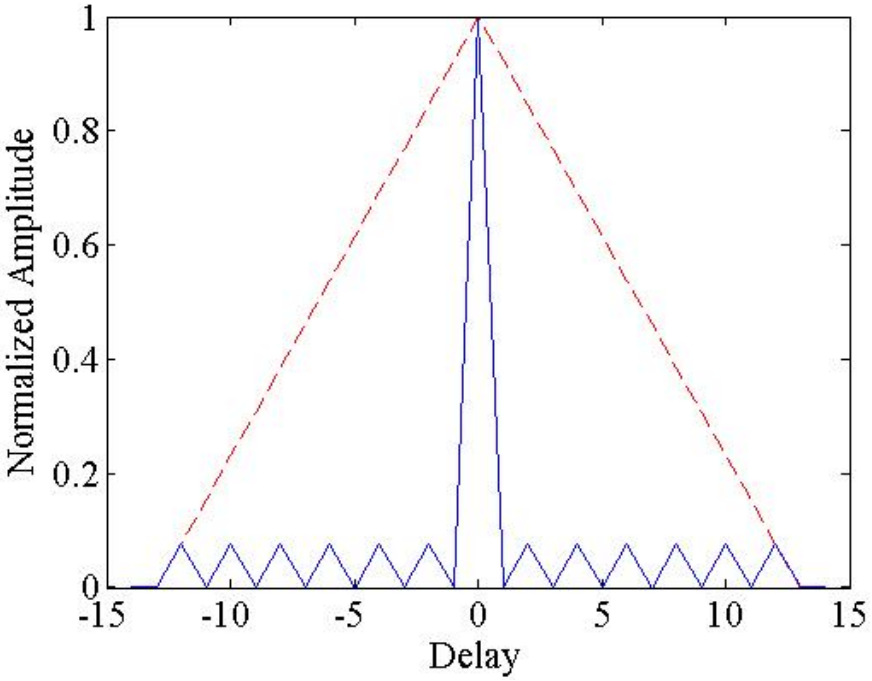

Figure 13: Auto-coorelation of the barker modualed signal (blue) and a unmodulated pulse (red). Auto-coorelation in time is the equivialent to the zero Doppler cut of the ambiguity function. [23]

3 Experimental HBR Receiver Hardware Setup

An experimental HBR Receiver has been developed in collaboration with FFI to detect targets of opportunity in the vicinity of the receiver location. Although targets could equally be detected around the transmitter site, given the properties of the HBR coverage as described in section 2.1.2. Data produced by this experimental receiver will be used to estimate the operational potential of HBR. The targets of opportunity are commercial airlines whose positions can easily be verified by their broadcasted ADS-B data.

The sensor system consist of a directional parabolic dish antenna mounted on a pan/tilt pedestal, which in real time can track commercial airplanes by their broadcasted ADS-B data or to be set to a fixed pointing position with an input of azimuth and elevation angles. A picture of antenna and pedestal is shown in figure 14. Tracking on ADS-B messages or on other secondary radar responses is not intended to have any operational purpose and is only used to secure maximum dwell time on target without the need of implementing advanced scan-on-scan techniques.

In addition to the described sensor system, the entire measurement system consist of a control PC, a superheterodyne receiver with IF-sampling, a GPS disciplined oscillator providing reference for synchronization and an ADS-B receiver providing real time target positions for tracking and for post-vertification of target detections. Data from measurements is recorded to a hard drive disk (HDD) for post-processing. An operational HBRR would however require real-time processing and some type of alert system or other forms of communication with an operator.

The choices of the HBRR components were heavily influenced by the availability in form of commercial off-the-shelf (COTS) components and shared use of equipment with an ongoing experimental research project at FFI. Only the front-end components and the FPGA-code, which was developed at FFI, were altered in respect of the other research project. As this HBR is tailored to the specific host on which it is intended to operate on, the front-end analog components restricts it from operating on other transmitters of opportunity. A schematic of the basic components of the complete system is shown in Figure 16

The receiver is measured to have an overall gain, G, of about 34dB and a system noise temprature, T_s, of about 1350K. The calculations and more detailed measurements can be found in appendix A. Some suggestions to improve receiver performance is presented in section 3.2.

Figure 14: Receiving antenna mounted on the P/T pedestal. Only one dish is used during experiments. Camera is used for true North referencing and video caption of targets.

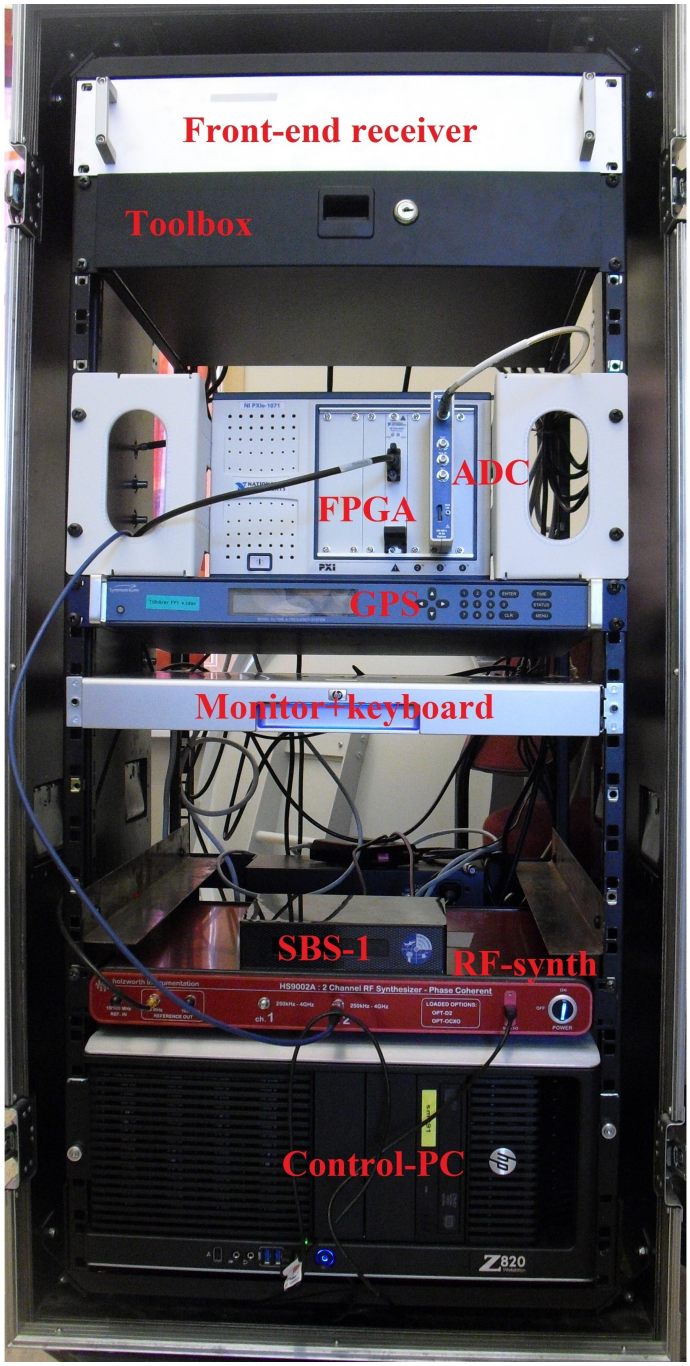

Figure 15: Rack with hardware components. From the top: Front-end receiver, toolbox, NI FlexRIO with FPGA and ADC modules, GPS clock, monitor with keyboard, SBS-1 ADS-B receiver, RF syntheszier, control and storage computer

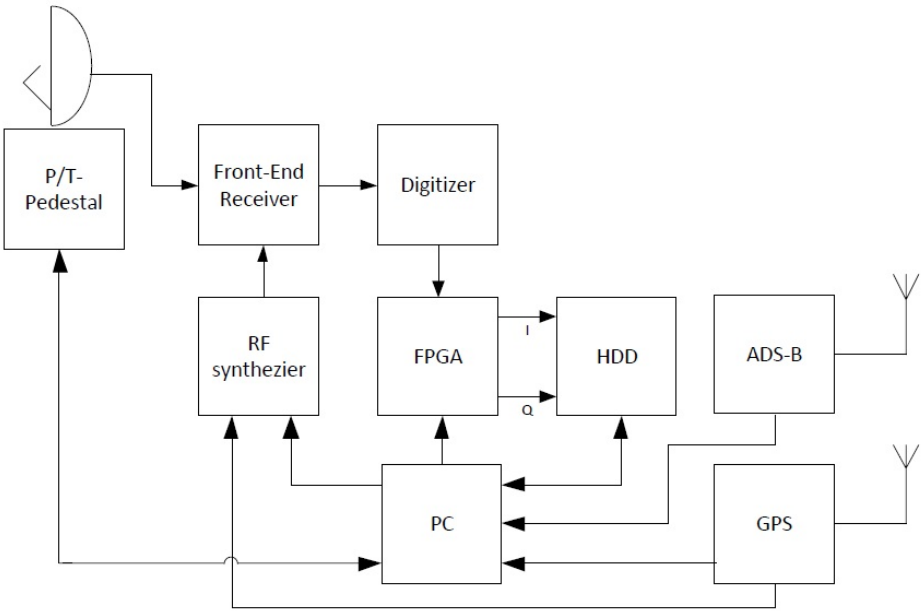

Figure 16: Schematics of the basic components of the experimental HBR receiver

3.1 The superheterodyne receiver

A supersonic heterodyne (superhet) receiver down converts a high radio frequency (RF) input into base band, directly or via one or more intermediate frequencies (IF), by mixing the RF with a signal from one or more Local Oscillators (LO). Almost all radar receivers operates on this superhet principle.[2, p.161] [22, p.6.1]. This HBR receiver has one analog IF stage which down converts a 1.3GHz RF into a 70MHz IF and a digital down converter (DDC) which converts the sampled IF signal into base band and splits the signal into I- and Q-parts. Although the first down-conversion is done with analog components, the IF-sampling classifies this receiver as a digital receiver.[22, p.25.1]

The front-end of the receiver includes the analog components from the receiving antenna up until the digitalization. The analog to digital converter (ADC), the DDC and other digital signal processing (DSP) parts is referred to as the back end of the receiver. The shematics of the superhet receiver are shown in figure17. The front-end components confiend in the rack are shown in figure 18.

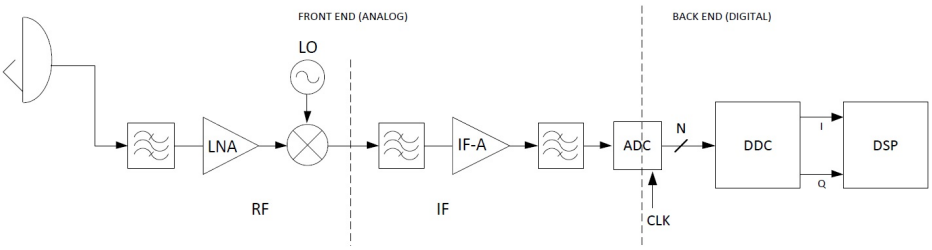

Figure 17: Schematics superhet receiver

The superhet receiver consists of the following components:

- Front end
  - RF section
    - Reflecting Parabolic Dish (QSR 700-OST)
    - Front end filter (FSY C1300-109-12SS)
    - Low Noise Amplifier (LNA) (Mini-Circuits ZX60-1614LN)
    - Local Oscillator (LO) (Holzworth HS9002A)
    - Mixer (Mini-Circuits ZFM-150)
  - IF section
    - 2 x IF band pass filters (Mini-Circuits SB-70+)
    - IF Amplifier (Miteq Au-1310)
- Back end/Digital section
  - ADC (NI 5762 250MS/s 16-bit Digitizer)
  - FPGA (NI PXIe-7962R)

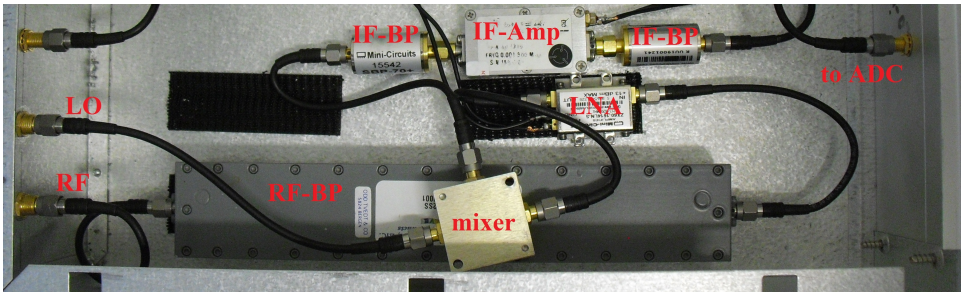

Figure 18: Front-end components

3.1.1 Analog Front-End Section

Following the signal path, the front-end of the receiver begins with the receiving antenna which uses a reflecting parabolic dish with a diameter (D) of 70cm. At a frequency of 1.3 GHz which corresponds to a wavelength (λ) of 0.23m, the half power beam width (HPBW) of the antenna is at least 23 degrees in vertical and horizontal plane and has a boresight gain of about 15dBi. These values are obtained by comparing with the radiation pattern of a uniformly illuminated circular aperture of same size. The radiaton pattern is calculated for the far-field region, also known as the Fraunhofer region, of the antenna. The far-field is defined [21] where the radius R from the antenna is

$$R \geq \frac{2D^2}{\lambda} \tag{29}$$

The radiation pattern of a circular aperture [14, p.334][23] is given as

$$E(\theta) = \pi(\frac{D}{2})^2 \frac{2J_1\left[\frac{\pi D}{\lambda}\sin(\theta)\right]}{\frac{\pi D}{\lambda}\sin(\theta)} \tag{30}$$

where J_1 is the Bessel function of the first kind and first order. The HPBW of the antenna can be approximated by the angle between boresight and the first null as illustraded in figure 19. This occure when the Bessel function is zero [14, p.334][23], which gives

$$\Delta\theta_{3dB} \approx 1.22\frac{\lambda}{D} \approx 70^\circ\frac{\lambda}{D} \tag{31}$$

Plot of the normilized power radiation pattern at the front of the antenna is shown in figure 19.

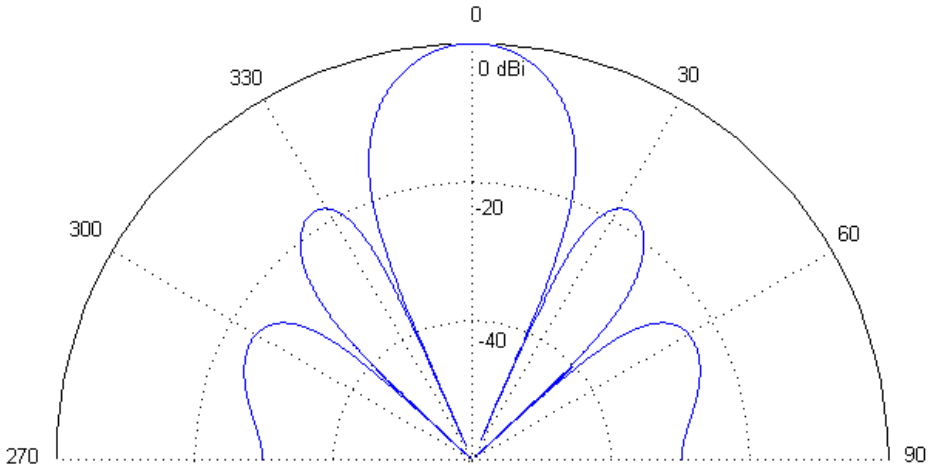

Figure 19: Radiation pattern for a uniform circular aperture with a diameter of 0.7m operating at a frequency of 1.3GHz

Since the parabolic dish is not a uniformally illuminated aparture, the true HPBW of the antenna is somewhat larger and the side-lobe levels is reduced because of attenuation of the edge illumination [18, p.754]. The boresight gain of the antenna can be found as

$$G_R = \eta \frac{4\pi A_a}{\lambda^2} \tag{32}$$

where A_a is the area of the antenna and η is the antenna efficiency factor, usually 0.55-0.60 for a parabolic dish [23].
The antenna is mounted on a pan/tilt pedestal, which can be set to a fixed elevation and azimuth position or to be set to follow commercial planes by tracking on their transmitted ADS-B data. Due to the pedestal's incapability of 360 degrees of rotation, there is a 20 degree blind zone where the beam cannot be centered. The antenna has two outputs; one for horizontal and one for vertical linear polarized waveforms. For the experimental measurements described in chapter 4, only the horizontal was used. From the antenna, a transmission line of 4 meters precedes the rest of the superhet receiver which is confined in the same rack as the control PC.
Using available COTS components in the operating frequency of the host (AN/FPS-110), a band pass filter with a -3dB pass band of approximately 100MHz is used as the front-end filter. The role of the front-end filter is to pass the wanted signal with low attenuation and reject unwanted signals from interfering in the mixing stage. Usually the front-end filter is placed in front of the Low Noise Amplifier (LNA) to prevent unwanted RF signals to overdrive the sensitive LNA. In areas with low probability of strong signal interference, the LNA can be placed in front of the RF filter to reduce the

overall noise figure. The LNA is, as the name suggest, an amplifier with a low noise figure and it is crucial for keeping an overall low noise figure throughout the receiver. Lowering the noise figure of the receiver will enhance the signal-to-noise ratio (S/N) of the HBR.
The mixer provides the down conversion from the high RF input to a lower IF. Simplified, the mixing stage can be seen as time domain multiplication of the RF input and the sinusoid from the LO. If the RF input is given by $\sin(2\pi f_{RF}t)$ and LO is $\sin(2\pi f_{LO}t)$ [2, p.164], then the first order products can be mathematically expressed as

$$\sin(2\pi f_{LO}t)\sin(2\pi f_{RF}t) = \frac{1}{2}\left[\cos(2\pi(f_{LO}-f_{RF})t) - \cos(2\pi(f_{LO}+f_{RF})t)\right] \quad (33)$$

where the required output is $f_{IF} = f_{LO} - f_{RF}$, while $f_{LO} + f_{RF}$ and higher order products needs to be filtered out by the IF-filter. The mixer is a double balanced mixer which uses four diodes that switch in pairs when the LO cycle goes from positive to negative and vice versa. This process can be approximated by mixing the RF with a square-wave LO and the output voltage can mathematically be described as multiplying a RF sinusoid with the Fourier series for the square-wave[8], which gives

$$\begin{aligned} V_{out} &= V_{RF}\sin(2\pi f_{RF}t)\left[\frac{4}{\pi}\sum_{n=1,3,5..}^{\infty}\frac{1}{n}\sin(n2\pi f_{LO}t)\right] \\ &= \frac{4V_{RF}}{\pi}\left\{\frac{1}{2}\left[\cos(2\pi(f_{LO}-f_{RF})t) - \cos(2\pi(f_{LO}+f_{RF})t)\right] + ...\right\} \end{aligned} \quad (34)$$

The minimum conversion loss is then given as

$$20\log_{10}(\frac{V_{RF}}{V_{IF}}) = 20\log_{10}(\frac{2}{\pi}) = 3.92dB \quad (35)$$

Equation 34 and 35 assumes perfect impedance matching. Normally the conversion loss is between 5 and 8dB. The conversion loss of the mixer in use is specified to be 6.7dB. The noise figure of a passive mixer at normal operating temperature is usually close to the conversion loss if no serious degradations is caused by i.e image noise fold-over and LO phase noise. Using a double sided mixer, frequencies on both sides of the f_{LO} gets down converted to the IF as shown in figure 20

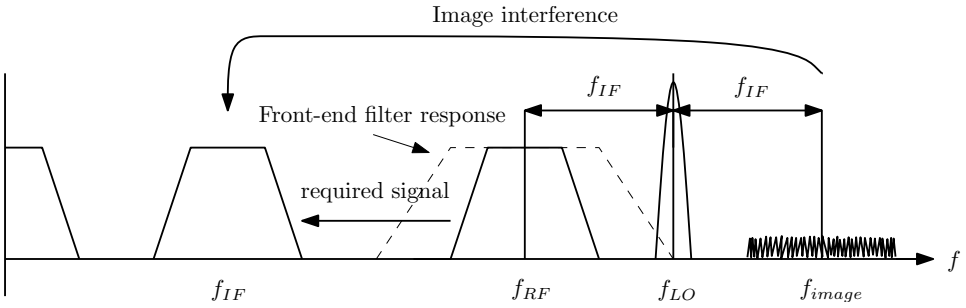

Figure 20: Down conversion in the frequency domain. The illustration is based on figures in [2, p.165] and [4, p.231]

The image signal f_{image} when $f_{LO} > f_{RF}$ is given as

$$f_{image} = f_{LO} + f_{IF} = f_{RF} + 2f_{IF} = 1318 + 140 = 1458 \pm B_n \text{MHz} \quad (36)$$

where $B_n = 2.2$MHz is the receiver bandwidth. To avoid image noise fold-over, the front-end filter must sufficiently attenuate the image frequencies. Thus resulting in this requirement of the relation between the front-end filter bandwidth (RF_{band}) and f_{IF} [2, p.165]:

$$RF_{band} \leq 2f_{IF} \quad (37)$$

As a real band pass filter response is not of an ideal rectangular shape, the requirement in equation 37 is an absolute minimum to provide any rejection of the image noise. The image noise fold-over can in worst case degrade receiver noise figure by 3dB. A solution is to select a high IF, but since cost of high performance filters increases with its operating frequency there will be a trade-off to be made between the advantage of using a low and high IF. A higher IF it will also require a higher sampling rate from the ADC given the Nyquist-Shannon sampling theorem (if bandwidth sampling is not applied). An IF of 70MHz is chosen as it meets the requirements in equation 37 and because of availability in COTS components. From measurements of the front-end filter, an IF of 70MHz will provide 80dB attenuation of the image noise. To achieve an IF of 70MHz the frequency of the LO is set as

$$f_{LO} = f_C + f_{IF} = 1318MHz + 70MHz = 1388MHz \quad (38)$$

The LO frequency is provided by a RF synthesizer which allows for fine frequency tuning. When operating, the f_{LO} is set at fixed frequency which require the oscillator in the host providing the transmitted frequency (f_C) to

be stable enough to avoid signals from drifting out of the receiver bandwidth (B_n).
At the output of the mixer, inter-modulation products causes spurious signals [8]. A spurious chart, as shown in Figure 21, is useful to identify the spurious frequencies that need to be rejected by the IF-filter and that no spurious products lie within the signal band, which is 2,2MHz at the center of the IF. In this case $f_{RF}/f_{LO} = 1318 \pm 1.1/1388 = 0.95 \pm 0.001$ and $f_{IF}/f_{LO} = 70 \pm 1.1/1388 = 0.05 \pm 0.001$. With this set up, the closest spur is from the inter-modulation product of the second harmonics of LO and RF ($2LO - 2RF = 140$MHz) and will be properly attenuated by the IF-band pass filter.

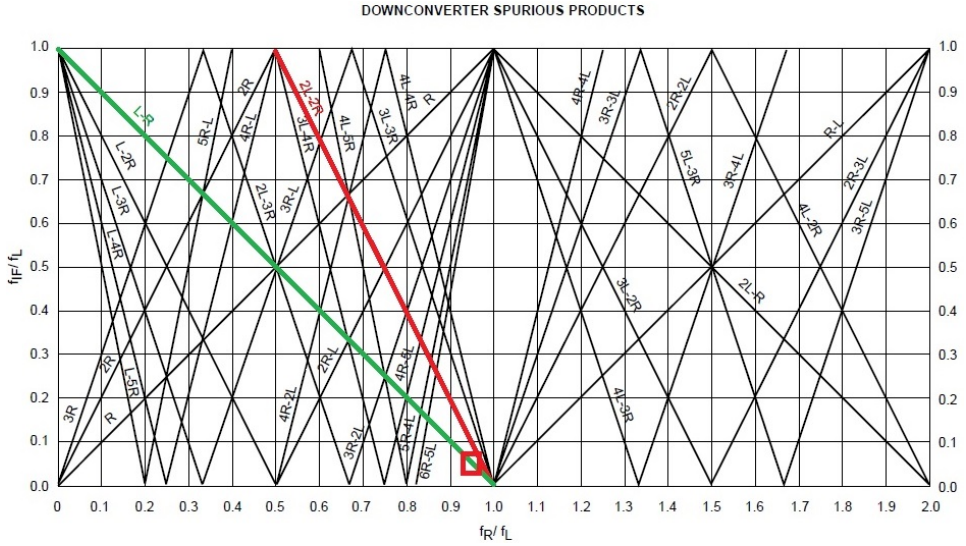

Figure 21: Spurious Products up to 6. harmonics[8]. Red square marks the required IF. The required output product is marked with green and the closest spur is marked with red.

The IF stage consists of a band pass filter, amplifier and then another band pass filter. The IF-Amplifier stage provides the overall noise figure and signal-to-noise ratio of the receiver before digitalization.

3.1.2 Digital back-end section

The back-end of the receiver consist of an ADC and a FPGA module from National Instruments (NI). The ADC samples at 16-bit providing a theoretical dynamic range of $20\log_{10}(2^{16}) = 96dB$. However, due to ADC-induced errors, the actual dynamic range is about 84dB [22, p.25.10]. Since pulse compression is applied after digitization, the pulse compression gain (PCG) of about 10dB (see section 2.3) is not restricted by the dynamic range of the ADC as the bit-resoultion can be increased by DSP. The ADC handles

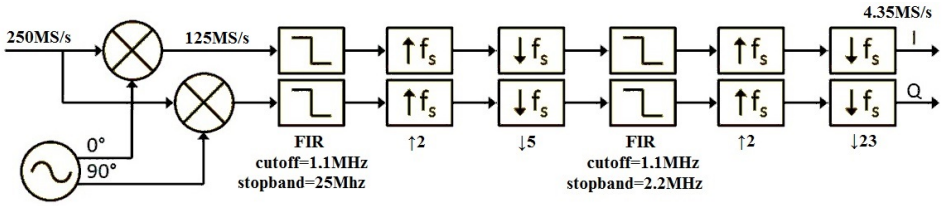

Figure 22: Schematics of FPGA code

peak-to-peak input voltages up to 1.9V.
The FPGA-code is written in LabView and developed at FFI after the recommendations given in NI homepages [10]. The ADC samples the IF signal with a rate of 250 MS/s. The FPGA generates an oscillator which provides a frequency matching the f_{IF} that mixes with the sampled signal to down convert and form I/Q data at baseband with a rate of 125MS/s for each channel. Each channel is then applied two stages of low pass FIR filtering, interpolation and desimation to acheive a double sided passband of 2.2MHz at a sampling rate that matches the transmitted pulse compression code by a factor x2. Basic schematics of the FPGA code is given i figure 22. The I/Q data is then recorded to HDD for post-processing. The FPGA records data as fixed-point values of the signal voltage seen at the ADC input. The conversion loss of the entire digital section is measured to be 0.6dB.

3.2 Overall Performance of the HBR Receiver

To calculate the expected coverage area of the HBR, a good estimate of the system noise temperature T_s of the receiving system is required. T_s is measured in Kelvin and is used in the bistatic range and radar equations, given in section 2.1.2 (equations 6 and 8). The receiver is measured to have an overall gain, G, of 33-34 dB and a system noise temprature, T_s, of about 1350K.

The system noise temperature can be divided into[15, 405]

$$T_s = T_a + T_{tr}(L_r - 1) + L_r T_0 (F - 1) \tag{39}$$

where T_a is the effective antenna temperature, T_{tr} is the temperature of the transmission line between the antenna and the rest of the receiver, L_r is the transmission line loss and F is the overall noise factor of the rest of the receiver components. The noise factor F is defined as the ratio between input and output (S/N)

$$F = \frac{(S/N)_i}{(S/N)_o} \tag{40}$$

and the equivalent noise temperature T_e of F is given as[2]

$$T_e = T_0(F - 1) \tag{41}$$

Parameter	DS max	DS min	Close Target	Far Target
$R_T(km)$	60	60	60	60
$R_R(km)$	-	-	2	150
$G_R(dB)$	15	-5	15	15
$\sigma_B(m^2)$	-	-	100	10
$F_T^2F_R^2(dB)$	-65	-65	0	0
$S/N(dB)$	48	33	67	15
$P_{in}(mV_{peak})$	16.7	1.7	148	0.4

Table 4: Estimated signal power and ADC input voltage for the experimental set-up location at FFI

where $T_0 = 290K$ which is used as the reference temperature. The noise factor for the cascaded components in the receiver is calculated using Friis formula for noise factor, which is

$$F = F_1 + \frac{F_2 - 1}{G_1} + \frac{F_3 - 1}{G_1G_2} + \cdots + \frac{F_n - 1}{G_1G_{2n-1}} \tag{42}$$

where F_n and G_n is the noise factor and power gain of each component and the subscripted number states the components appearance in the chain when following the path of the input signal. From equation 42 it becomes evident that a LNA with a high gain (G_1) and low noise factor F_1 early in the cascaded chain will give a low overall noise factor if the noise factors of the first components are minimized. The overall gain of the cascaded chain is obtain by simply multiplying the gain of each component as

$$G = G_1G_2 \ldots G_n \tag{43}$$

Gain/loss and noise figure for each component in the superhet receiver is obtained from datasheets and measurements with a spectrum analyzer with network analyzing capability. The noise factor for a passive devices is approximated to equal the loss L, which is the inverse of gain ($L = \frac{1}{G}$). This is true when the passive device is operating at physical temperature equal to T_0. Components datasheet figures and own measurements are organized in excel spreadsheets along with the bistatic radar equation in order to estimate HBR performance. Screenshot from these calculations is given in the appendix. The overall gain of the receiver is measured to be G=33.7 before sampling and with a system noise temprature, T_s, of about 1350K.

An estimation of the excpected S/N and the peak voltage at ADC input for the experimental HBR set-up described in chapter 4 is given in table 4

The peak voltage V_{peak} at the input of the ADC (P_{in}) is calculated as

$$P_{in}(V_{peak}) = \sqrt{2P_RGZ_0} \tag{44}$$

Where P_R is given in Watts and G is the overall gain of the receiver, Z_0 is the receiver impendance=50 Ohm and $\sqrt{2}$ is for conversion from V_{rms} to V_{peak} which is given as $V_{peak} = \sqrt{2}V_{rms}$ and where the conversion from power in Watts to RMS voltage is given as $V_{rms} = \sqrt{P(W)Z_0}$. P_R is the power received from the output of receiving antenna and is calculated by eliminating the receiver noise from the bistatic radar equation in equation 8 which results in

$$P_R = \frac{P_T G_T G_R \lambda^2 \sigma_B F_T^2 F_R^2}{(4\pi)^3 R_T^2 R_R^2 L_T} \tag{45}$$

All the equations in this section, along with the bistatic radar equation, is incorporated in Microsoft Excel spreadsheets to calculate the expected preformance of the HBR receiver. The outlay of these spreadsheets is given in the appendix B.3
Some suggestions for improvements is made in case of further development of this expermental HBR receiver or for anyone who wish to build a similar receiver. A LNA with higher gain, as long as it does not overseed the dynamic range of the ADC, would improve the overall noise figure, even with a noise figure higher then the LNA in use. Calculations with a LNA with a $G_1 = 30$ and noise figure of 1.5dB is given in appendix and estimate to produce a about $T_s = 650K$ resulting in an inprovement of 700K or about 3dB. Further image rejection can be achieved by a more narrow RF-filter, (although there is usually a trade-off in band pass filters between low attenuation and narrow bandwith), an additional image rejection filter before mixing, selction of a higher IF or using an image rejection mixer.

3.3 P/T pedestal and ADS-B tracking

The receiver antenna is mounted on a pan/tilt pedestal (2B PT-3002) that allows for two-axis rotation in azimuth and elevation and can be set to track commercial airplanes in real time by their broadcasted ADS-B data, or to be set to a fixed pointing position with an input of azimuth and elevation angles. A SBS-1 receiver and software from Kinetic Avionic is used to acquire aircrafts ADS-B positions and a log of the ADS-B data is kept to verify target detections. Software written in LabView developed at FFI [9] converts the ADS-B positions of a selected target into a range azimuth elevation (RAE) vector from the receiver site. The pedestal operates by serial communication (RS-485 Pelco-D protocol) and is capable of absolute position feedback. To track targets, the LabView code developed at FFI, is modified to send commands to steer the antenna towards the target position by comparing the RAE vector and the pedestal feedback position. A discrete proportional regulator is used to regulate the rotational velocity. The feedback position

of the pedestal pointing direction is continuously logged along with target position.

4 Experimental Measurements

A measuring campaign has been conducted with the experimental HBR described in chapter 3 in order to measure the performance of the HBR in real life scenarios. The HBR sites, located at Kjeller (R_X) and Kongsvinger (T_X), was evaluated in the term project [23] and found to be a reasonable location for experimental measurements. Commercial aircrafts are used as targets of opportunity and detections are verified by ADS-B data. Due to the close proximity to Oslo Airport at Gardermoen, targets of opportunity are plentiful.

The HBR host is defined as cooperative but non-dedicated. It is co-operative in the sense that information about PRF, signal waveform and physical behavior of the transmitting antenna is available, but is considered non-dedicated as its operations is solely for own monostatic radar purposes and that no changes is applied to enhance HBR capabilities. Due to the surrounding terrain, R_X and T_X is not within direct LOS. Although no straight line path exist between R_X and T_X, the location is found adequate for RF synchronization based on one way path loss estimations. As time and phase synchronization is done with direct signal measurements, signal processing described also applies to non-cooperative hosts, both friendly and hostile, if waveform and basic antenna operations can be measured or otherwise predetermined. Since the direct/diffracted signal from the transmitter can been seen throughout the entire scan area of the receiving antenna, synchronization is possible without a dedicated reference antenna.

The measuring campaign is divided into two parts; measurements of the direct signal and measurements of targets of opportunity. For direct signal measurements, the receiver antenna is fixed to point at the transimtter site. For target measurements, the antenna is set follow a selected target of oppertunity. Section 4.4 shows how the host's PRF, scan-time and HPBW can be obtained by direct signal measurements. While only post-processing is applied for these measurements, implementation for an operational HBR is discussed.
Based on measurements presented in section 4.5, the estimated range of this HBR is about 180km for commercial airliners within LOS of both transmitter and receiver.

4.1 Basic operational properties of transmitter and receiver

The transmitter, an AN/FPS-110, is a long range air surveillance/defence radar, which during the measurements emitted pulsed binary phase modulated (Barker-13) signals with a stable PRF of about 325Hz and has carrier frequency of about 1.3GHz. The bandwidth of the pulsed signal is about

2,2MHz which, after pulse compression, gives a theoretical minimum range cell width of approximately 140m in the monostatic region and increases with the bistatic angle as illustrated in figure 3. The half power beam width (HPBW) is approximately 1.5 degrees in azimuth and considerable larger in elevation. The large elevation angle characterizes this transmitter as 2D radar incapable of measuring altitude of targets. The transmitter antenna rotates clockwise with a constant scan time of about 12 seconds. For target rangeing and location, the scan time and the PRF is measured by analyzing the direct signal. The PRF must also be continuously measured to compensate for drifting in the unsynchronized oscillators in the transmitter and receiver. High accurate real time synchronization with the direct signal might be challenging as the direct signal is only detectable in part of the transmitter's scan area. The variation of the PRF as seen by the HBR receiver can be reduced by synchronizing the transmitter and receiver with the same reference, i.e. with GPS-time or via a direct link.

The receiver utilizes a reflecting parabolic dish with a HPBW of about 25 degrees in azimuth and elevation. Maximum attenuation by antenna directivity is about 10-15dB resulting in poor to no angular resolution of strong signals. For direct signal measurements, the receiver is fixed to point at the transimtter site. For target measurements, the antenna follows the target for maximum dwell time. The direct signal can be measured throughout the entire possible scan area of the receiver, which means there is no need for a dedicated reference antenna to measure the direct signal from the transmitter. More details about the HBR receiver is given in chapter 3.

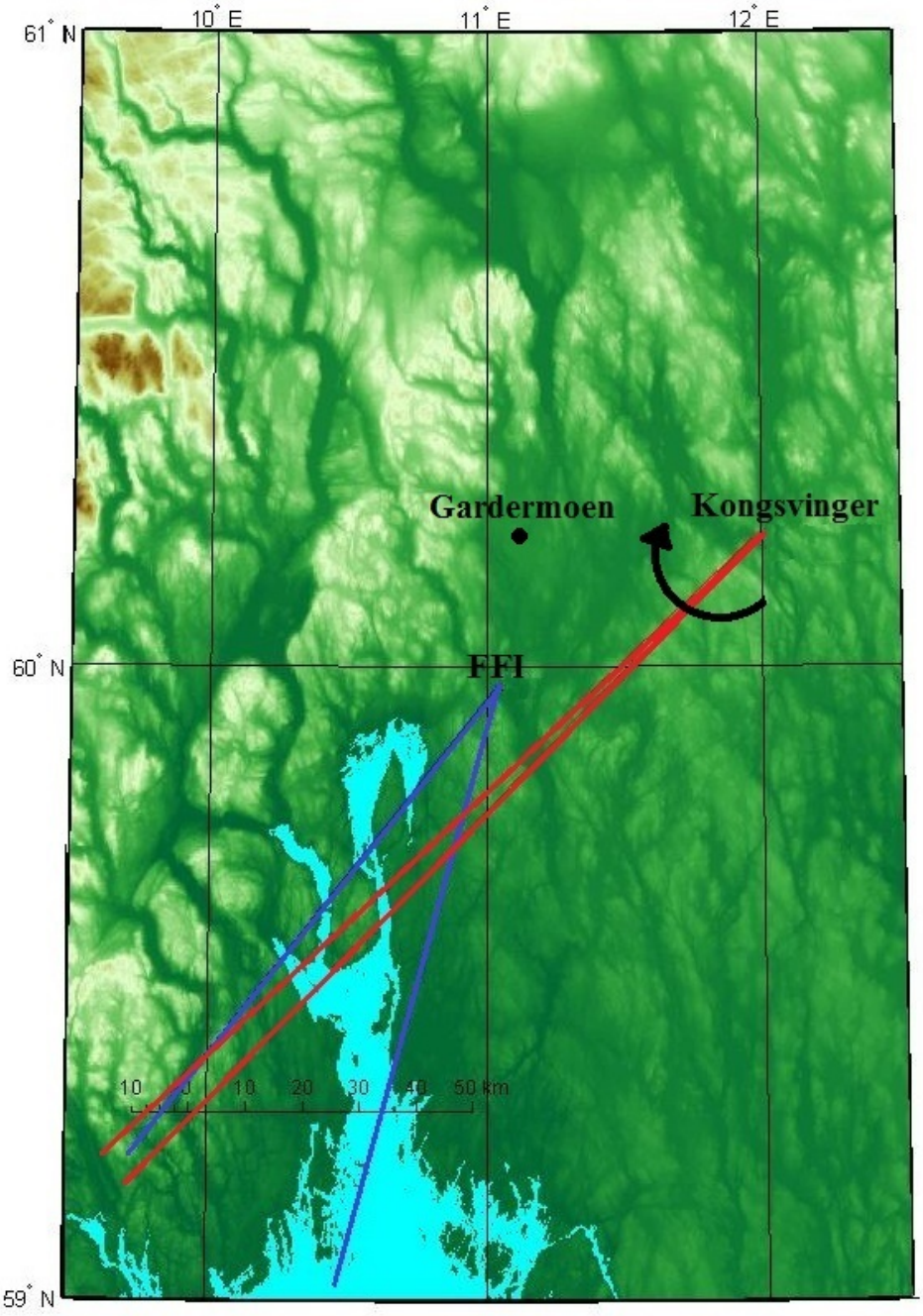

Figure 23: Experimental HBR locations with illustrated half power antenna beam

4.2 Set-up Locations

The HBR receiver is located at FFI in Kjeller, hitchhiking on a cooperative, but non-dedicated air surveillance/defence radar at Kongsvinger. At this location, the close proximity to Oslo Airport at Gardermoen provides plenty of targets of opportunity in the vicinity of the receiver location. Figure 23 shows the geographic locations of transmitter, receiver and Oslo Airport at Gardermoen in a topograhic map.

With this set-up, the baseline (L) is, as defined in section 2.1, approximately 60km. At a receiver altitude (h_R) of about 150m and transmitting altitude (h_T) of about 350m, L is well within the requirement for direct signal synchronization stated in section 2.1.2, which from the equation 12 is

$$L \leq 130(\sqrt{0.15} + \sqrt{0.35}) = 127km \tag{46}$$

However, due to the terrain profile between T_X and R_X, the direct signal path is not in direct LOS and therfore heavily diffracted. In order to estimate if the receiver can detect the diffracted signal, the total diffraction loss from transmitter to receiver is calculated with a Matlab function implemented at FFI. This function use a multiple knife-edge diffraction algorithm with parameters from ITU-R P.526-10 and a terrain profile which is generated from a Digital Terrain Elevation Data (DTED) of level 1, which has a Cartesian grid resolution of about 90x90m. More on this function can be found in [17].

Figure 24 shows the path loss caused by diffraction due to the terrain profile.

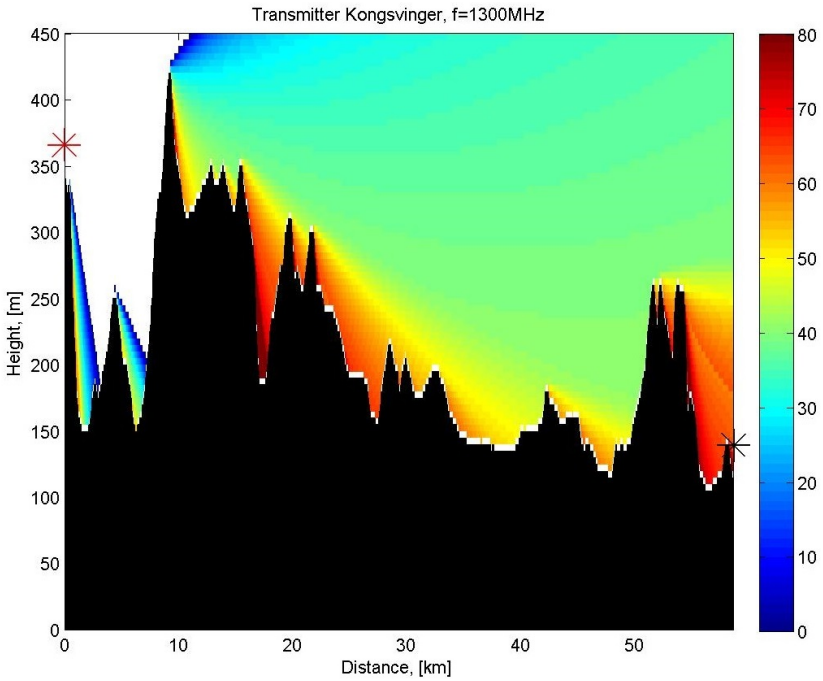

Figure 24: Diffraction loss (dB) form T_X (red cross) to R_X (black cross). Adopted from [17].

The S/N of the direct signal is estimated by adapting equation 8 for a one way path between T_X and R_X which gives

$$(S/N)_{DS} = \frac{P_T G_T G_R \lambda^2 F_T^2}{(4\pi)^3 R_T^2 k T_s B_n L_T L_R} \approx 48dB \tag{47}$$

where the propagation factor of direct signal, due to diffraction loss between transmitter and receiver, is caculated to be $F_T^2 = -65dB$. The rest of the parameters is given in appendix B.3. Equation 47 presumes maximum antenna gain for both transmitter and receiver, which means this equation is only valid when the antenna is physically pointing at eachother. As the receiver has a maximum attenuation of 10-15dB in directivity, the direct signal is expected to be detectable throughout the scan area of the receiver. The transitter antenna has however a much higher directivity, allowing DS synchronization only when the receiver is within the main lobe of the transmitting antenna pattern.

The required target altitude for direct LOS from both transmitting and receiving sites, is shown in figure 25. These constraints was found in a term project [23] and the figure is replicated here with the heading translated for convenience. The bistatic LOS constraints is caused almost exclusivly by the LOS from the receiver site.

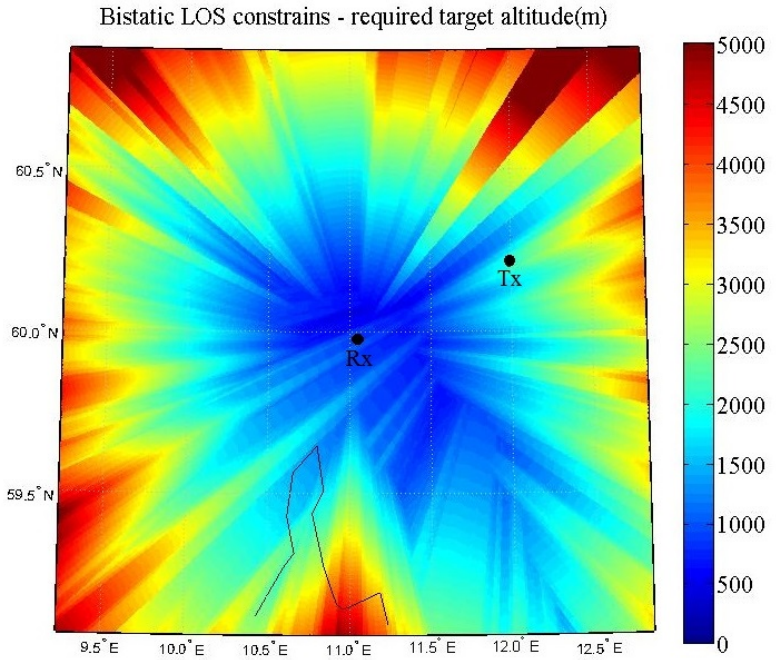

Figure 25: Required target altitude (m) for bistatic LOS [23]

4.3 Noise measurements

The noise floor is measured after applied pulse compression and with no pulse integration. A histogram from a 500x500 sample patch of a synchronized time-range matrix containing nothing but noise is used to produce the amplitude distribution plot in figure 26 . These distribution plots shows the characteristics of white noise, with a uniform phase distribution and a Rayleigh distribution of the RMS voltages as described in section 2.2. From these data a noise floor of $0.5V_{rms}$ or -53dBm is set. This noise level is used in S/N calculations when no pulse integration is applied.

4.4 Direct Signal Measurements

With the transmitter and receiver not in direct line-of-sight (LOS) of each other, the direct signal used to synchronize the HBR is a diffracted and most likely also a multipath version of the emitted signal. Although this raises some challenges it has some advantages as well. The advatage beeing reduced ground clutter and direct signal interference masking target echoes. The distinct DS can also ease scan-time measures. The dissadvatage is an increased requirement in clock stability as synchronization can only be acheived from scan to scan. There will also be parts of the scan time where no DS or stationary clutter exist for phase synchroniation.

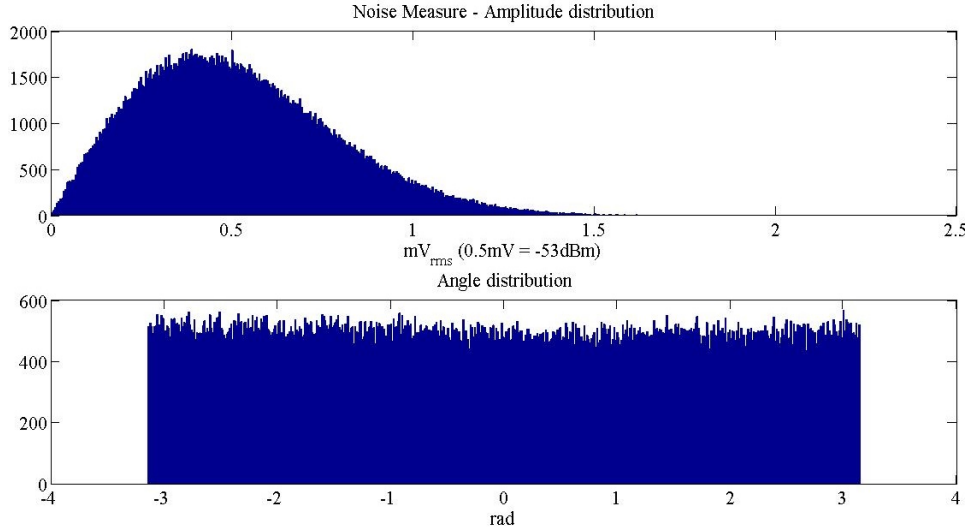

Figure 26: Noise measurements after pulse compression

Accurate synchronization with the direct signal is needed to provide time synchronization for determining range and angular position of a stable scan time transmitter. Phase synchronization for MTI or Doppler processing usually requires a higher accuracy than what is set for time synchronizaiton. In this experiment the synchronization update time (T_u) is set by the scan time of the transmitter.

4.4.1 Identifying the direct signal

As the host is a long range radar with a low and constant PRF, there will most likely be a period with only noise prior to the arrivel of the DS pulse. (Although a precaution has to be made of the unlikely event of a strong reflector, at very high altitude or if over the horizon propagation is occruing, is present near the unambiguous range of the HBR.) This will allow for simple identification for time synchronization when the DS is detectable. Figure 27 shows the measured signal power as the transmitting beam sweeps over the receiver site.

The characteristic sinc-form from the horizontal antenna pattern of the transmitter is seen in the upper plot as the transmitter beam passes the receiver site. In the bottom plot the direct signal, with the familiar pulse compression form (see figure 13), with noise on the left side and clutter scatters to the right. Time is obtained by dividing samples (n) with the sampling rate (Fs).

$$\text{time(s)} = \frac{n}{Fs} \tag{48}$$

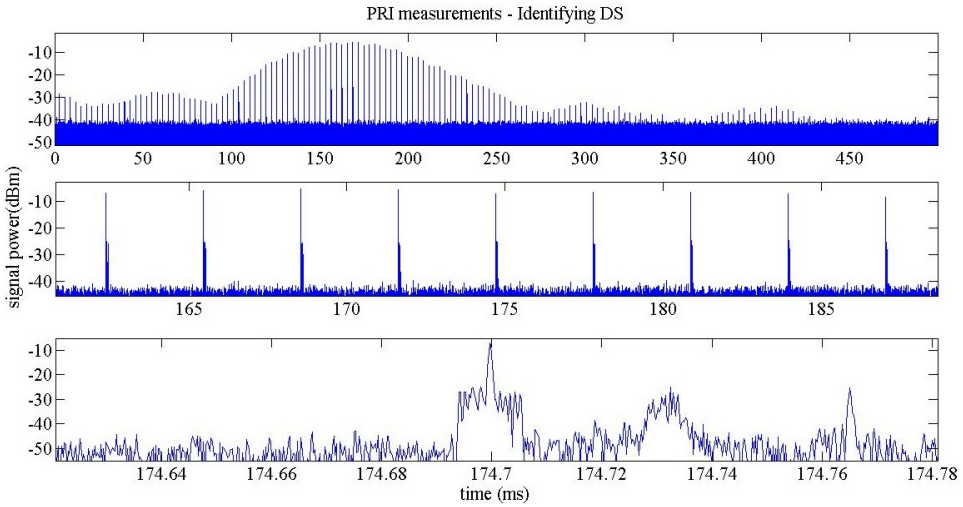

Figure 27: Measurements of the DS as signal power vs. time. The upper plot graph is increasingly zoomed in at the middle and bottom plot.

Time between direct signal pulses is the pulse repetition interval (PRI) which is the reciprocal of the PRF.

$$PRI = \frac{1}{PRF} \tag{49}$$

Synchronizing with DS sets the zero bistatic range ($R_T + R_R - L$) at arrival of the DS. With synchronized PRF, the bistatic range is determinable as time from last DS to target echo (Δt_{rt}) multiplied with the propagation speed (c). Using equation 50 in section 2.1.2 to solve for the bistatic range leads to

$$(R_T + R_R - L) = c\Delta t_{rt} \tag{50}$$

Distance between DS provides the unambiguous range of the HBR as described in section 2.1.2. Figure 38 shows a time-range intensity plot where the bistatic range of each pulse is aligning in a matrix χ. "Negative" range is included to show the side lobes of the strong DS.

4.4.2 Scan-time measurements for improved target location

The receiving antenna provides poor angular resolution, and is therefore not sufficient to locate targets more accurately then on a large part of a iso-range contour. As the HPBW of transmitter is much smaller, synchronization with the pointing direction can improve target location. However, as described in section 2.1.5, the bistatic angular resolution will be less, as the directivity of

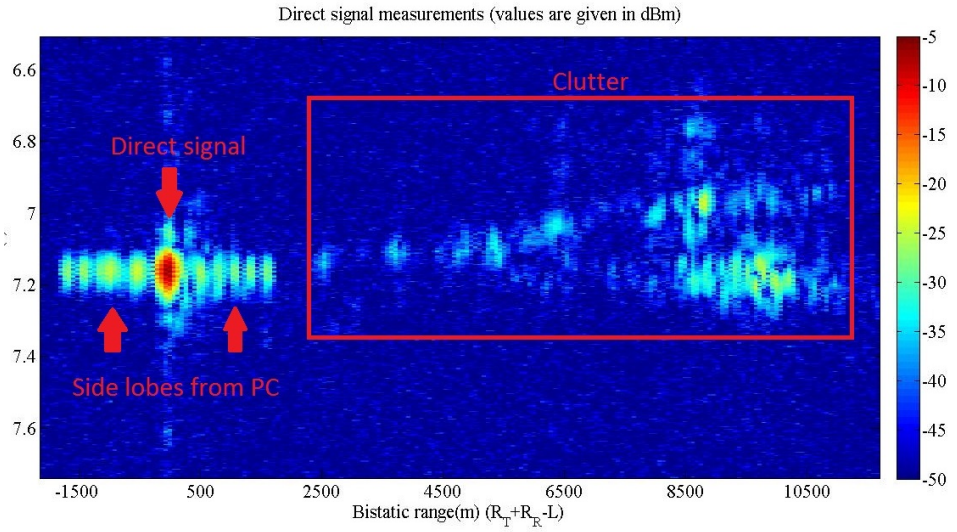

Figure 28: Intensity plot over time vs. Bistatic range

the transmitting beam is only applied in one way path compared to the two way rejection at the sides seen by the monostatic radar. When operating with a stable scan time and from a known location, the azimuth position of the transmitter can be determined by time relative to the strongest direct signal in a scan which is when transmitting beam aligns with the baseline between T_X and R_X. Scan time is measured between the peaks in figure 29.

The azimuth angle of the transmitter (A_T) can then be calculated as

$$A_T(\text{deg}) = A_{TR} + 360\frac{\text{time after peak DS (s)}}{\text{scan time (s)}} \tag{51}$$

where A_{TR} is the azimuth direction from T_X to R_X in a true North referance and where scan time is predetermined as

$$\text{scan time (s)} = \frac{\text{number of pulses between peak DS}}{PRF} \tag{52}$$

If scan time is known, the angular resoultion of the transmitter can be found by measuring the signal power of DS pulses as the transmitting beam passes the receiver. Figure 30 illustrates the 3dB and the 6dB beamwidth.

The transmitter HPBW is required to approximate the target resolution as described in section 2.1.5.

4.4.3 Phase Measurements for Coherent Processing

Phase synchronization is needed for coherent processing, like MTI or Doppler processing, which can be used to reject stationary clutter. Also,

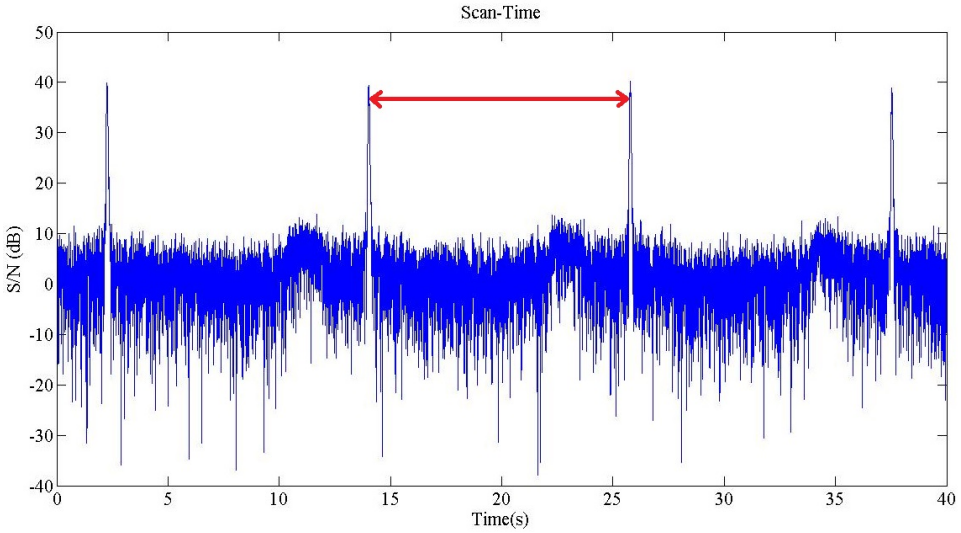

Figure 29: Cut at zero bistatic range of the time-range matrix to illustrate scan time

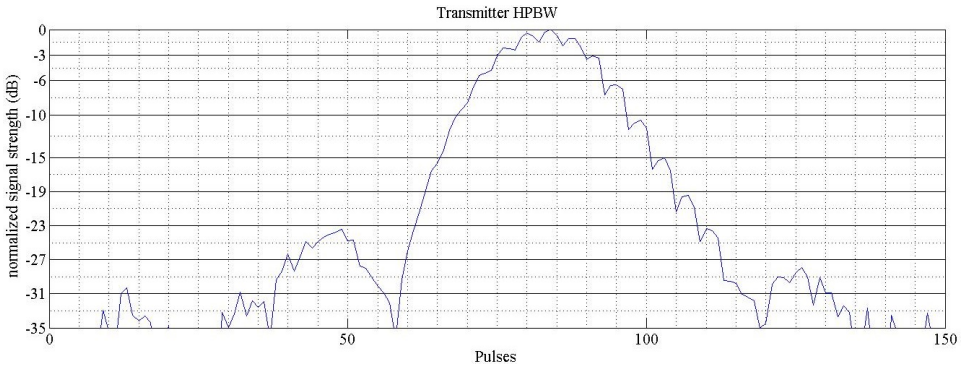

Figure 30: Comparing several DS pulses to measure transmitter beamwidth

if a target is non-fluctuating from pulse-to-pulse, coherent integration can theoretically improve S/N (in power) by a factor as much as the number of integrated pulses (n_P). However, coherent processing requiers high accurate phase synchronization in addition to high stability and low phase noise [26] in transmitter and receiver oscillators. If the HBR configurations allows for pulse-to-pulse phase-synchronizing, i.e. with a stable clutter seen throughout the scan-time, the required clock stability [26, p.261] is $\Delta\phi/2_c\Delta t_{rt}$, where $\Delta\phi$ is allowable phase error in radians, f_c is the carrier frequency and Δt_{rt} is time between received direct signal and target echo. For indirect synchronization i.e. with GPS time disciplined oscillators, the required clock stability becomes $\Delta\phi/2_c$, where$T$ is the coherent integration time. If only phase synchronization is achieved every scan-time, the required stability for the clocks increases with the update time T_u.
In this experiment, the direct signal is only detectable at every scan time and no stable clutter can be seen throughout the scan time. Direct pulse-to-pulse phase synchronization is therefore not viable with this set-up. However, study of the pulse-to-pulse phase at zero bistatic range of the time-synchronized matrix χ indicates an approximately consistent phase over the direct pulses when the transmitter beam sweeps over the receiver. Figure 31 shows the unwrapped phase of each pulse at zero bistatic range when transmitter is pointed towards the receiver site. Here we see no coherency in phase from the noise of the sidelobe nulls of each side of the DS pulses, while the phase becomes linear or consistent throughout the high powered DS pulses. As the direct signals is not expected to cause any Doppler shift, the slant slope seen in figure 31 indicates an offset frequency that needs to be corrected for.
If the phase is consistent, then coherent processing can be applied. Factors that have contributed to this coherency are the short duration this is seen, a stable PRF from the transmitter, time synchronization with the sampled direct signal and stable clocks in the receiver. Although this might not be a reliable coherent system, the coherency shown in figure 31 allows for coherent processing techniques with data from this experiment to be demonstrated in section 5.3.

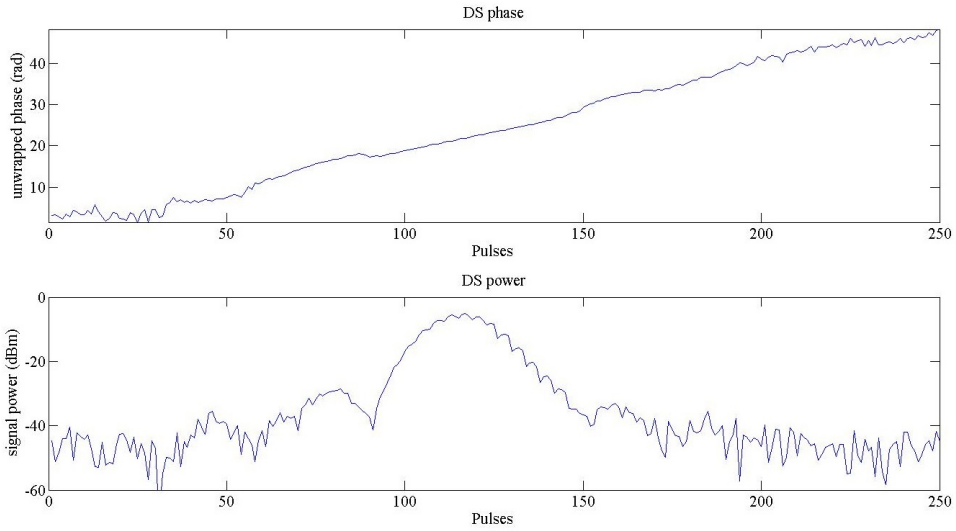

Figure 31: Unwrapped phase (rad) of time synchronized DS pulses. The slant slope of the unwrapped phase indicates a consistent offset in frequency.

4.5 Target detections

For target measurements, the receiving antenna is mounted on a pan/tilt pedestal (described in section 3.3) set to track a specific aircraft in order to provide maximum target dwell time and minimum rejection from the directivity of the receiving antenna. Since the direct signal from the transmitter can been seen throughout the entire scan area of the receiving antenna, synchronization is possible without a dedicated reference antenna.

4.5.1 Detection verificatian through ADS-B reference

ADS-B is a surveillance technology used in ATC where aircrafts is broadcasting, among others, their current position. Using the ADS-B receiver and software described in chapter 3, logs all the commercial aircrafts in the vicinity of the receiver. To be comparable with the target measurements, targets positions are converted to bistatic range ($R_T + R_T - L$) from the receiver site. Figure 32 shows a time-range plot with target ADS-B posistions in colored squares contected with dotted lines. The signal power intensity is illustrated in grayscale to enhance the visibility of the ADS-B plots. Figure 33 show multiple target detection in one scan and their geographical posistions. This illustration shows how aircrafts in close vicinity is detected outside the HPBW of the receiving antenna. The use of targets broadcast positions is primarily for experimental purposes. However, ADS-B comparsion may have operational value if considering an HBR concept where the receiver is set only to report detections of targets whitout ADS-B positioning.

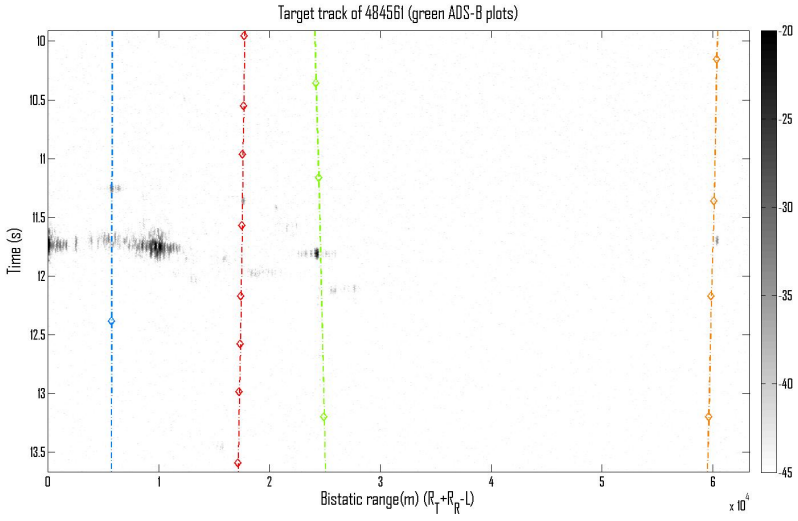

Figure 32: Time-range plot with ADS-B plots

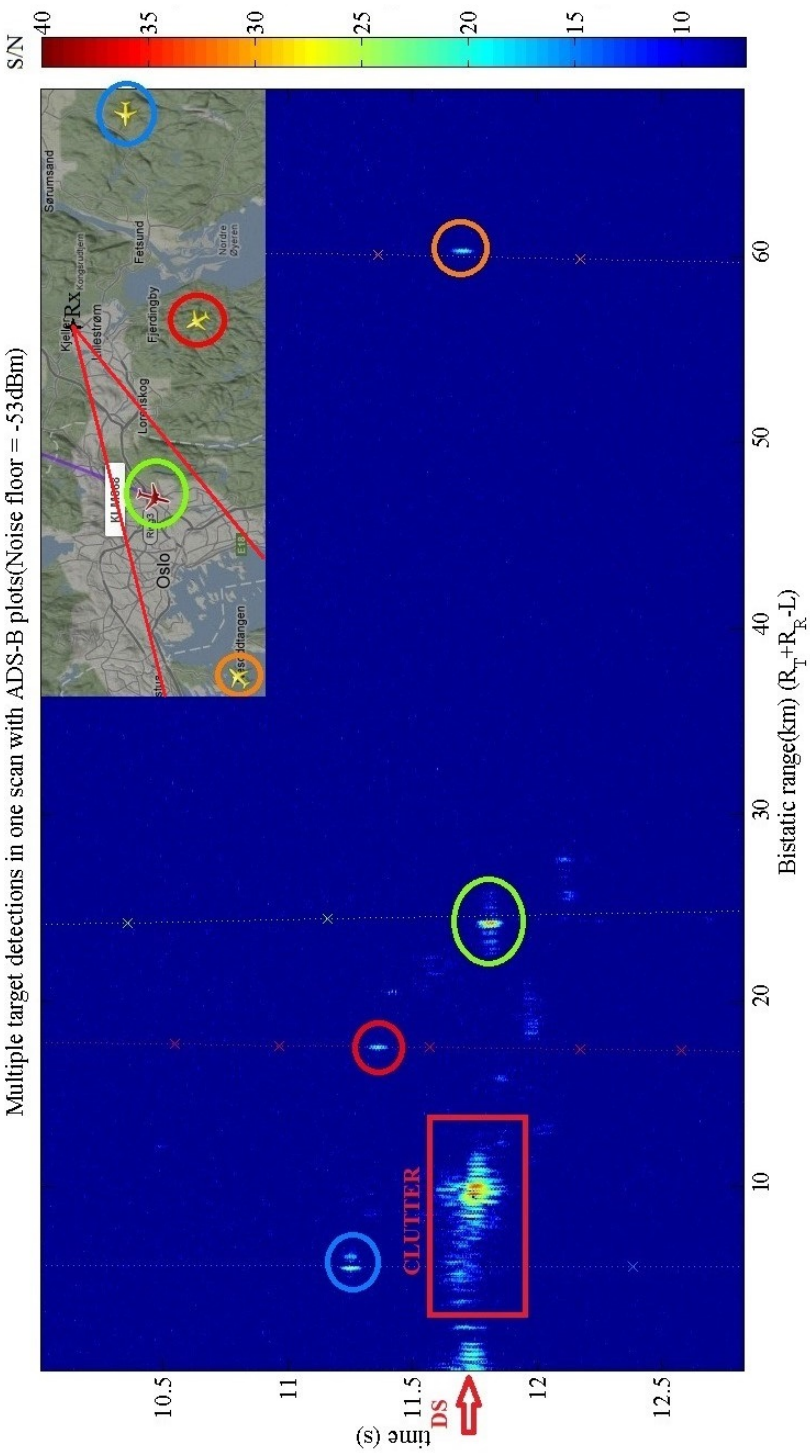

Figure 33: Time-range plot with ADS-B data showing multiple target detections in one scan. (Background of upper right image courtesy of Flightradar24.com)

4.5.2 Range Estimation

In order to estimate the maximum range of the experimental HBR, a target was tracked over a period of time after passing the receiver site heading South-West. The target was a Boing-777 aircraft at a cruising altitude of about 10km above ground level. S/N is measured from maximum target signal in each scan after pulse compression. No pulse integration methods have been implemented in this dataset. Figure 34 show the S/N from the target as a function of the bistatic range along with a relative function of the bistatic range loss ($R_T^2 R_R^2$). The range loss is calculated with the targets true position data, based on the ADS-B log. A table with the measured target S/N and the bistatic distances is given in appendix B.4.
Unfortunately the recording was stopped while the signal was still detectable. An estimation based on the expected range loss suggest that the target would be detectable with a S/N of 15dB at ca. 300km bistatic range ($R_R + R_T - L$). An oval of cassini at this distance can be approximated by a circle centered on the halfway baseline with a 180km radius ($\frac{R_R+R_T}{2}$). Measurements from this target are used to verify the parameters set to estimate the coverage area of this HBR. Using the parameters given in appendix B.2 results in an approximately mean value for this target RCS of about $50m^2$.

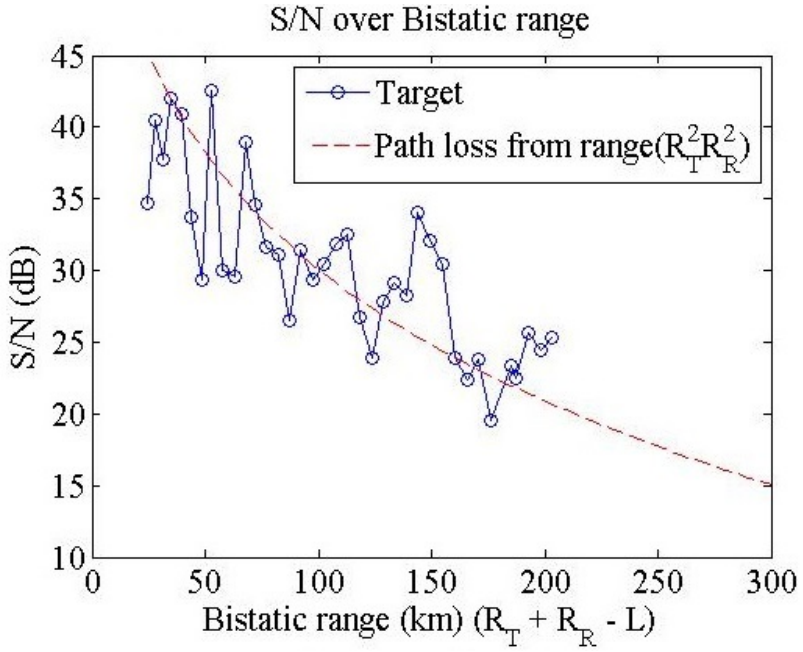

Figure 34: Measured S/N of target is in blue and the dotted red line shows relative S/N loss caused only by $R_T^2 R_R^2$ in the bistatic radar equation

5 Digital Signal Processing Techniques

In this chapter the measurements from the experiment is used to demonstrate digital signal processing (DSP) techniques that will improve HBR performance. Pulse compression was applied on the measurements presented in chapter 4. While non-coherent integration can more easily be achieved, the possibilities of a coherent radar include greater improvement in detection by clutter rejection and increased S/N. However, coherent processing requires accurate phase synchronization, which may be challenging to achieve with HBR. These processing techniques is a step towards bringing the overall detection, false alarms and the clutter rejection to an acceptable level that is required of a HBR to function as an operational radar.

5.1 Pulse compression

The basic principles of the Barker coded pulse compression was presented in section 2.3. With the experimental HBR, the barker coded waveform was known. If the transmitter is non-cooperative, the transmitted waveform can either be obtained by studying the direct signal or using the direct signal as a reference signal for the match filter. If the waveform is unchanged, a more robust template could be made from a number of consecutive pulses.

To apply pulse compression, the I/Q data generated by the FPGA is converted to a complex signal ($z(n) = I(n) + jQ(n)$). The barker code however, can be described by a real amplitude as the phase shift is either 0 or 180 degrees ($e^{j0} = 1, e^{j\pi} = -1$). As real numbers is its own complex conjugate, the matched filter is simply the time reversed of the transmitted signal. The pulse compression was preformed with discrete convolution in time, which can be expressed as

$$z_{pc}(k) = \sum_{n} z(n) B_{13}(k - n + 1) \tag{53}$$

Where $B_{13} = 1, 1, 1, 1, 1, -1, -1, 1, 1, -1, 1, -1, 1$ and each Barker bit is represented by two samples as the sampling rate is twice the chip rate (see section 3.1.2). If the matceh filter is long, then the more computational efficient multiplication in the frequency domain, by using Fast Fourier Transform (FFT) and Inverse FFT (IFFT), is preferred. For real time processing a FIR filter made with the Barker coefficients could also be used as a matched filter.
For the Barker-13, the sidelobe reduction which can be achieved is $20\log_{10}(13) = 22,3dB$ and the pulse compression gain (PCG) is $10\log_{10}(13) = 11,1dB$. Figure 35 show a range cut of a direct signal pulse with and without applied pulse compression. The form of the pulsed compressed signal is recognizable from figure 13. As the figure illustrates, the

noise in the pulse compressed signal is raised. A window function could be applied to suppress sidelobes, but the PCG and S/N will naturally remain the same.

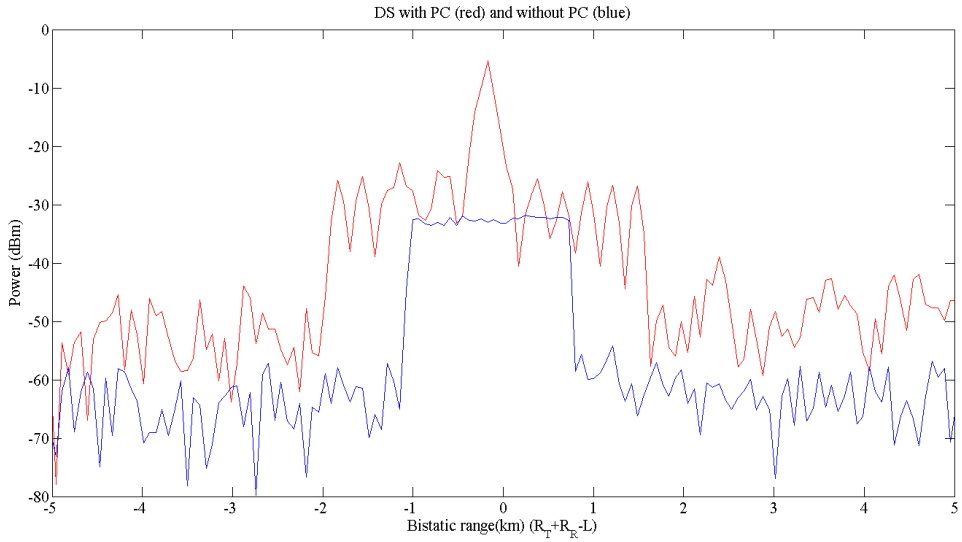

Figure 35: Pulse compression applied on real data, where the red curve is the matched filter response, while the blue curve is the amplitude response of the Barker code.

5.2 Pulse integration

From the time-range matrix presented in figures 32 and 33 from section 4.5, the target signals was visible in several consecutive pulses. Pulse integration is a method on which target detection is determined on the basis of more than one pulse. For the monostatic radar the number of pulses to integrate is usually taken as the number of pulses a target is illuminated by the half power beamwidth of the transmitting antenna ($\Delta\theta_T$). The time a target is in $\Delta\theta_T$ is usually referred as dwell time, which with a stable scan time and short dwell time compared with target velocity, can be found as time the transmitter takes to rotate one $\Delta\theta_T$. If $\Delta\theta_T$ is given in degrees the dwell time is the transmitter scan time multiplied with $\Delta\theta_T$ divided by 360. The number of pulses during this dwell time is set by the PRF as

$$N = \frac{\text{scan time} \times \Delta\theta_T(deg)}{360} = \frac{12 \times 1.5 \times 325}{360} = 16 \tag{54}$$

This method of determining N is not analogous to the HBR, since the directivity and look angle of receiving antenna will influence target dwell time. However, since the target was tracked with a wide angle receiving antenna, $N = 16$ is applied in this section.

Figure 36 illustrate the effects of noise reduction with pulse integration. The scale of the mV-axis is set by the highest value and the mean value is also referred to in power (dB). We see the mean value is reduced with coherent integration, while the non-coherent integrated noise is about the same, but here the standard deviation is reduced. The plots are based a histogram generated from a patch of 200x200 samples of noise is taken from $|\chi|$, $|\chi_{ni}|$ and $|\chi_{ci}|$. Where χ is the complex time-range matrix from the measurements, χ_{ni} is applied non-coherent integration as

$$\chi_{ni} = \frac{1}{n_P} \sum_{k=1}^{N} |\chi_k| \tag{55}$$

and where χ_{ci} is applied coherent integration as

$$\cdot\chi_{ci} = \frac{1}{n_P} \sum_{k=1}^{N} \chi_k \tag{56}$$

Non-coherent integration returns the mean value of the envelope of N pulses, which will reduce the variance of uncorrelated additive noise. Target S/N improvement with non-coherent integration is a function of P_D, P_{FA} (see section 2.2) and N and can be described by the Albersheim approximation given in [13, p.49]. Figure 37 shows a range-cut where a target is seen, and shows the reduction in noise variance compared to the non-integrated vector. The target peak is about the same for both, about 25dB, but the local sidelobes is reduced by 3-4dB by applying non-coherent integration compared with the no integration. However, also the clutter is seen integrated out of the noise, and for proper clutter suppression, a coherent processing technique will be demonstrated in section 5.3. Following Levanon's [13] notation and logic, the coherent integration of N pulses, the noise power can be reduced by a factor of N [13, p.46]. Target S/N improvement with coherent integration depends on the coherency of the target returns. If accurate phase synchronization could be applied, the S/N power ratio for N pulses could improve as much as factor N. Coherent processing can also benefit with clutter rejection. In section 5.3, coherent integration is demonstrated with pulse-Doppler processing, where also clutter suppression could be achieved if the target is moving.

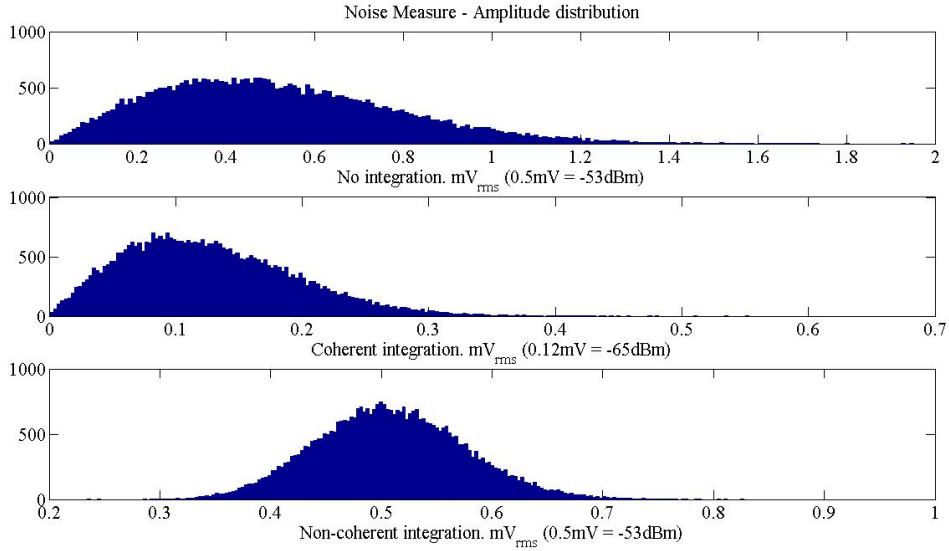

Figure 36: Pulse integration effects of the noise

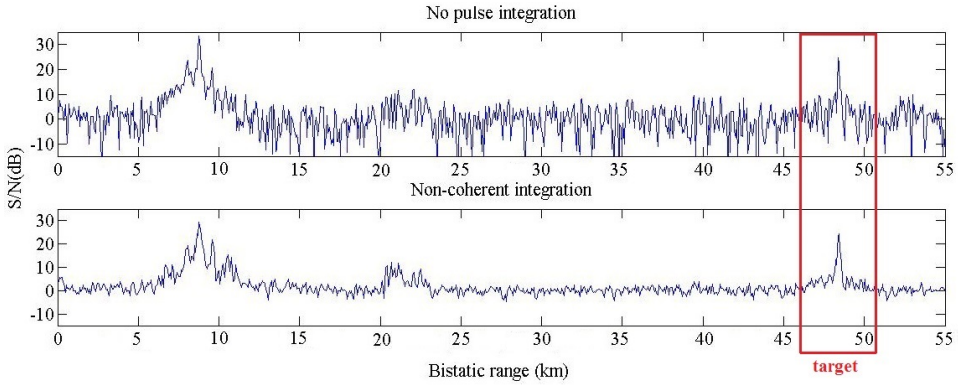

Figure 37: Range cut from time-range matrix, target marked in red square.

5.3 Pulse-Doppler Processing

As described in section 2.1.4, the Doppler shift observed in the receiver can be used to separate moving targets from stationary clutter. This can be achieved with pulse-Doppler processing if the radar is coherent. Coherency in pulsed radars requires high synchronization accuracy which can be challenging with a HBR. Experimental measurements, where the phase is consistent throughout the direct signal pulses (figure 31), is used to demonstrate how clutter suppression can be achieved with a phase synchronized HBR. Pulse-Doppler processing is described in detail by Olsen [17] and the work in this section is based on this thesis.

The PRF synchronized time-range matrix (χ) is transformed to frequency domain as a Doppler-range matrix (χ_{rd}). This is preformed with a FFT-function in Matlab which can mathematically be expressed with the discrete Fourier transformation (DFT) as

$$\chi_{rd}(m,n) = \sum_{k=1}^{N} \chi(k,n) e^{(-j2\pi/N)(k-1)(m-1)} \tag{57}$$

where N is the number of pulses to integrate. N relates to the integration time T as $T = N \times \text{PRI}$.
Phase synchronization can be achieved with direct or indirect methods as described in section 4.4.3. For direct pulse-to-pulse synchronization, the complex conjugated of a range cell known to have a strong stationary signal is multiplied throughout the range cells for direct phase compensation. This can be expressed as

$$\chi_{rd}(m,n) = \sum_{k=1}^{N} \chi(k,n) e^{(-j2\pi/N)(k-1)(m-1)} \chi^*(k,C) \tag{58}$$

where C is a constant range cell number of a direct signal or strong clutter echo. With indirect synchronization, a constant frequency offset can cause stationary clutter to be perceived as a moving target. In the experimental data, there was a small offset in frequency. Since the offset is constant, the phase error will be linear and could therefore be compensated with a linear function $y(k)$ of the offset phase where the direct signal is not seen. When y(k) represent the phase, the complex conjugated signal needed for phase compensation could be expressed as $e^{-jy(k)}$. Using the same DFT expression, this type of phase compensation gives

$$\chi_{rd}(m,n) = \sum_{k=1}^{N} \chi(k,n) e^{(-j2\pi/N)(k-1)(m-1)} e^{-jy(k)} \tag{59}$$

A time-range patch (χ), from the experimental measurements, is used to illustrate two beneficial aspects of Doppler processing; improved S/N from the coherent integration and clutter suppression. Figure 38 shows an intensity plot of χ where two target echoes is seen, one strong inside clutter at roughly 7km and one weaker at a larger bistatic range i.e. just below 4km.

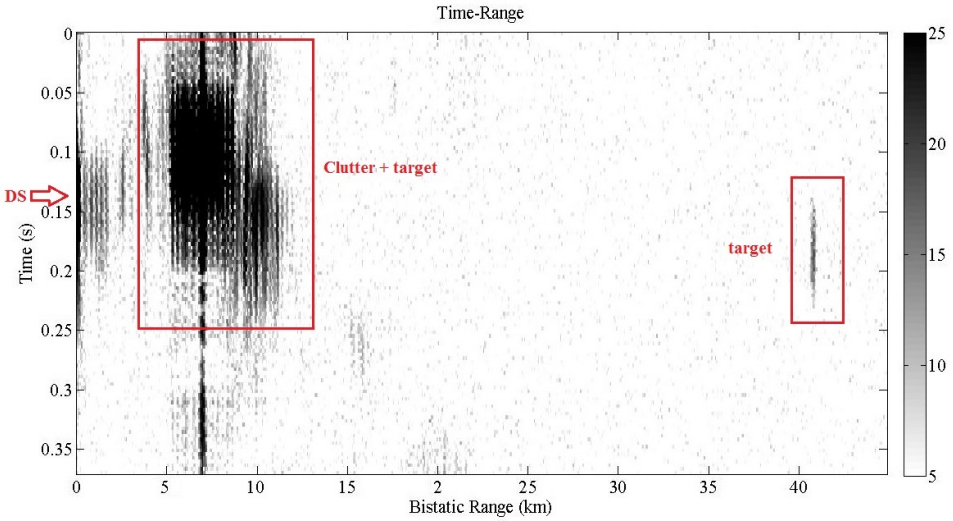

Figure 38: Time Range

First, $y(k)$ is obtain by using linear regression on the unwrapped phase of the direct signal pulses as seen in figure 39. Figure 39 also show how the corrected phase of the direct signal becomes stationary after correcting for the offset frequency.

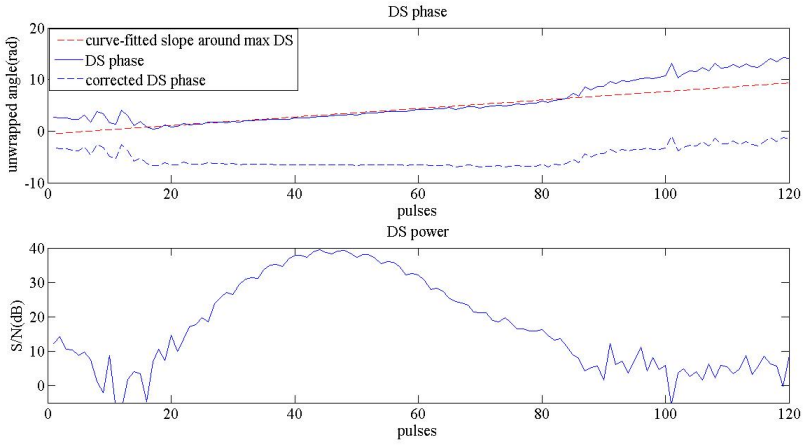

Figure 39: Linear phase correction

Pulse-Doppler is then applied on N=16 pulses over the far right target. Figure 40 show a time cut at the target range along with the unwrapped phase of this vector. The 16 pulses are marked with a red box, where the slope of the phase inside indicates a coherent Doppler shifted target return.

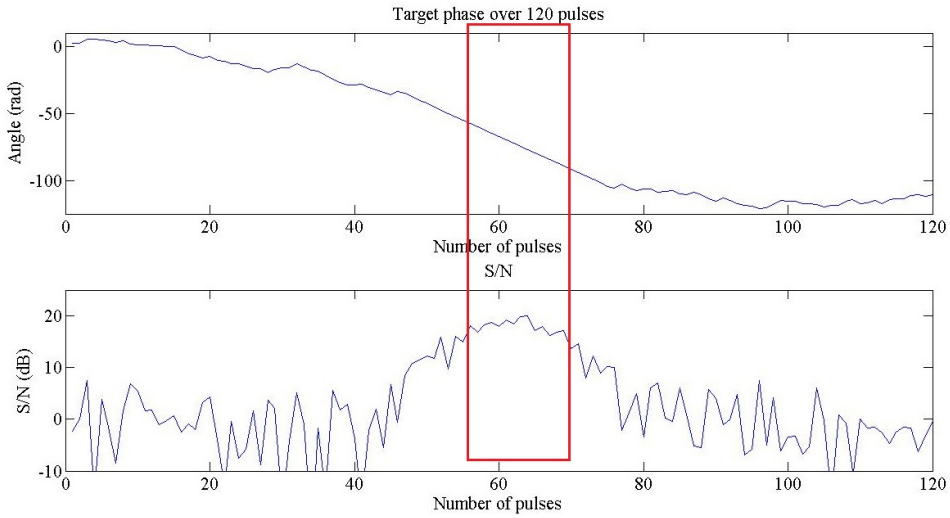

Figure 40: Target phase over pulses

The output Range-Doppler (χ_{rd}), shown in figure 41, illustrate how the moving targets is separated in frequency from the stationary clutter. To reduce the sidelobes in frequency from the strong target echo and the clutter, a window function could be applied.

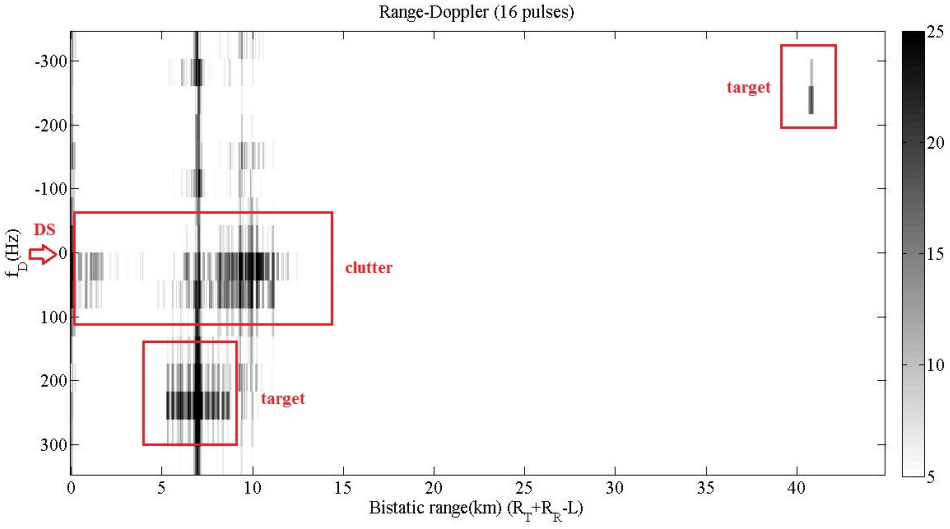

Figure 41: Range-Doppler plot with N=16 pulses

The choice of PRF and waveform is determined by the host and not a parameter of freedom for the HBR designer. If the transmitter uses a stable PRF, the maximum unambiguous Doppler shift can be exceeded and cause blind Doppler speeds. Blind Doppler speeds occur by ambiguous Doppler

shifts aliasing into the ”cutter zone”, which is the area around zero Doppler shift that gets rejected for clutter suppression. Low PRF and integration time T (which is the reciprocal of the Doppler resolution Δf_{D_B}, see section 2.1.4) will increase the probability of aliasing into the clutter zone, since the width of the clutter zone cannot be smaller than the Δf_{D_B}. The low, stable PRF and the short integration time of this particular experimental HBR may therefore not be favorable for Doppler processing in this aspect. However, while a target could maintain the exact blind Doppler speed on an iso-Doppler contour (which forms hyperbolas [26, p.122]) for one HBR, adding a second HBR receiver to the scene would resolve the blind speed. Overall, Pulse-Doppler processing will improve HBR performance by clutter suppression and increased S/N if accurate synchronization can be achieved.

5.4 Target Location

The accuracy on which one pulse target echo can be located is determined by the radar resolution. Given the poor directivity of the receiving antenna, the angular resolution of the HBR is improved by determining the azimuth position of the transmitting beam, resulting in a HBR radar resolution similar to the one illustrated in figure 8 in section 2.1.5. In section 4.4.2, based on the stable rotation of the transmitter, a way of estimate the azimuth angle of the transmitter beam as a function of time was established. Using this method, an azimuth-range matrix for one rotation of the transmitter antenna is generated and presented in figure 42.

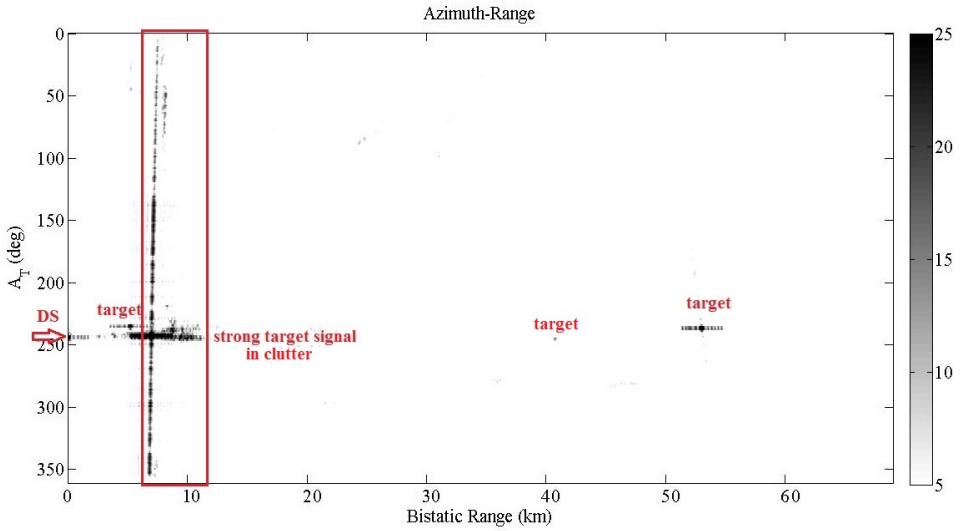

Figure 42: Azimuth-range

Until now, the target detections have been confined to a time/azimuth-range or Doppler-range matrix, but by solving for the bistatic triangle with the equations given in section 2.1.5, target detections is converted into Cartesian coordinates. A threshold is used to plot the detection in a Cartesian grid centered on the transmitting site shown in figure 43. This type of plots could be projected onto a map and updated for each scan. Figure 43 also shows how a close target with high RCS is visible in the transmitter's side-lobes throughout the scan-time, thus forming the familiar elliptic iso-range contour. These results lay a platform for further tracing of targets through multiple scans that will improve clutter rejection and allows for tracking algorithms to be implemented for greater accuracy in target location.

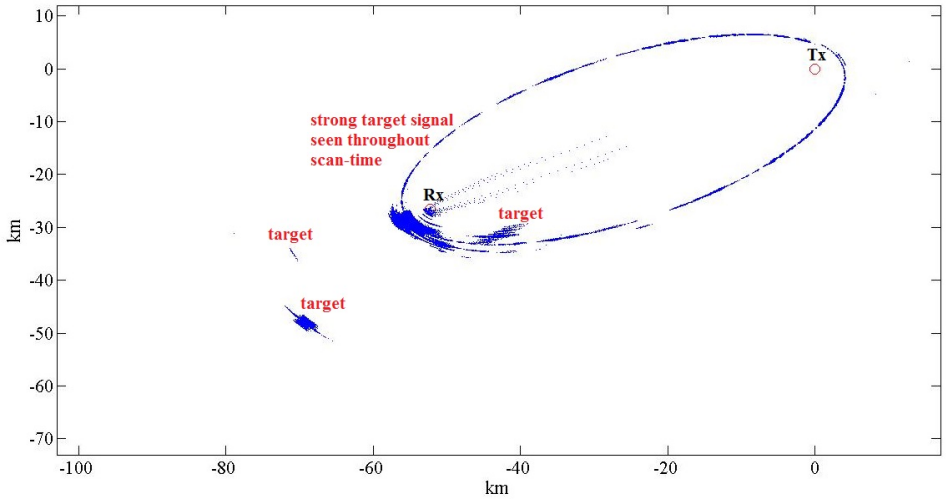

Figure 43: Detections from one scan converted to a transmitter centered Cartesian grid.

6 Future Perspectives and System Potential

Although HBR may prove advantageous with anti-jamming and counter-stealth capability in certain situations [26] [7][3] , such considerations will not be treated here. This discussion will mainly focus on HBR applications for homeland security, operating on existing hosts where covert operation is not required and that bistatic and monostatic target RCS is presumed to be of about equal size. With these restrains, the main advantage of HBR is low cost.

HBR applications depend on whether the host is cooperative or non-cooperative. With a non-cooperative host, the surveillance data of the host is usually not readily available, allowing the entire HBR coverage area to provide new and potentially useful information at a low cost. Whilst operating on a cooperative host, the HBR receiver can serve as an additional sensor augmenting the performance of the existing host by extending the coverage area, increase probability of detection and improve target localization.

6.1 Hitchhiking on a non-cooperative host

Non-cooperative radar can, in a military perspective, either be friendly or hostile, with the latter more unlikely within homeland security applications of the HBR. In this section, the host is considered to be friendly, while its surveillance information cannot be obtained otherwise and thus being a non-cooperative host.

Operations with a non-cooperative host require synchronization with the direct signal. This is performed in the experimental set-up described in chapter 4 and the methods is therefore applicable in operations with a non-cooperative host. As no surveillance information is shared by the host, the entire HBR coverage area provides surveillance information in areas that might not be covered by own sensors. An example of a HBR coverage area can be illustrated by using the experimental set-up. The coverage area at these sites is estimated with the LOS constrains found in [23] and the bistatic radar equation, where the parameters is based on the performance measurements of the experimental HBR. Figure 44 illustrate the HBR receivers coverage area for commercial aircrafts, which is expected to have a RCS of at least $10m^2$, at altitudes of 3km above sea level. With a detection threshold of 15dB, the coverage extends at least 100km from R_X. Because of the close proximity to T_X, the coverage area to is well within the coverage area of the host (which is not illustrated). In figure 45 target RCS is set to $0.1m^2$ and at an altitude of 1.5km. At this low-level height,

we see the LOS-constrains from figure 25 is reducing the coverage towards T_X, where dark blue indicates no coverage. Still, a range of about 20km from the receiver site is expected for these low-signature, low-level targets.

Challenges of operating on a non-cooperative host are accurate time/phase synchronization and the lack of control over the transmitter. Phase synchronization can be achieved if the direct signal, or a reflection from stationary clutter, can be used as reference throughout the entire scan time. However, this requires a close proximity and LOS between reference antenna and transmitter, which may result in strong direct signal interference. If localization is not necessary, detection of moving targets is still possible without any synchronization.

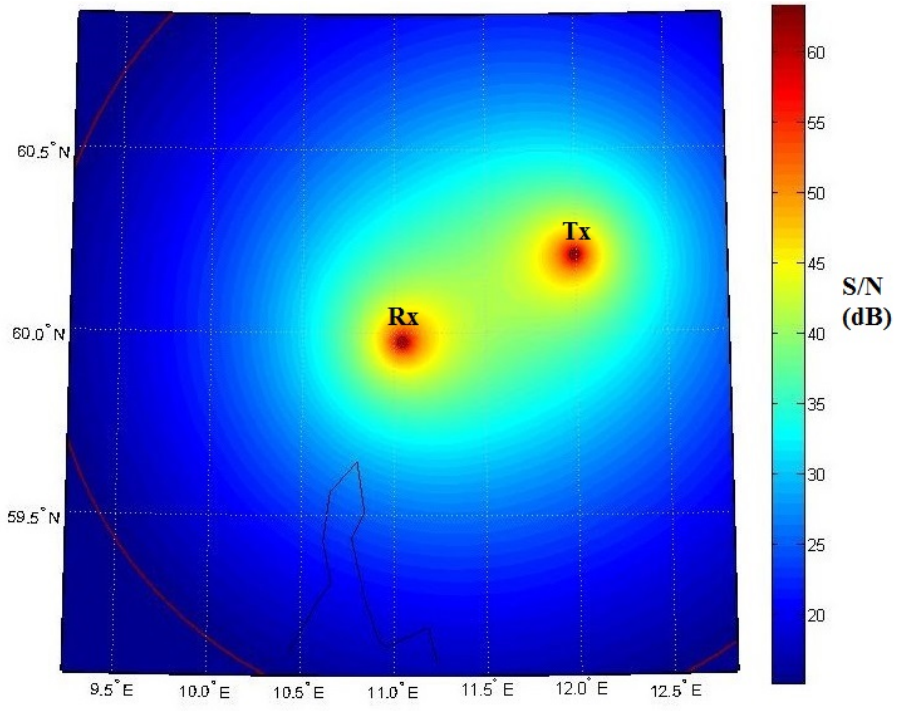

Figure 44: Coverage area for commercial airlines (RCS=$10m^2$) at cruising altitude (adapted from [23]).

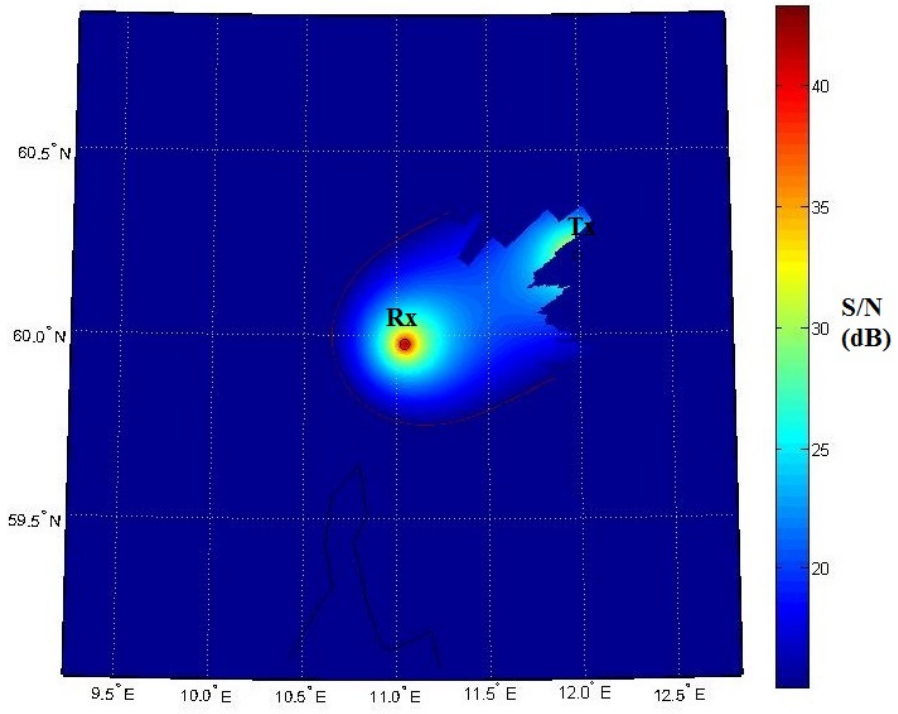

Figure 45: LOS constrained coverage area for low signature targets (RCS=$0.1m^2$) at altitude of 1500m (adapted from [23]).

6.2 Hitchhiking on a Cooperative Host

Hitchhiking on a cooperative host is considered to be a likely scenario for homeland security applications. All the non-cooperative HBR applications apply to the cooperative, with the addition of the possibilities for improved synchronization. The waveform and antenna operation is also available without direct signal measurements. Remaining on the premise of an existing host, the host is considered to be non-dedicated, in the sense that its operation is not intended for bistatic operations. However, a cooperative host may provide synchronization with only a minor modification. Enhanced synchronization, compared with the non-cooperative direct signal method, can be in form of a connected link or by indirect synchronization with GPS time disciplined clocks. If phase synchronization can be achieved, the HBR will inherit the advantages of coherent processing. This will also allow the HBR receiver to operate far outside the coverage area and no need for adequate LOS between host and receiver. However, LOS between transmitter-target and receiver-target is still required. Within a cooperative HBR application, target reports from the receiver can be netted with the host to augment probability of detection within the coverage area of the host or extend the detection range. This will then be a netted system where

the transmitter and receiver work closely together, maybe even allowing low level data sharing to be made, and thus inceasing the overall system detection performance. This has not been evaluated in this work, as the radar's (transmitter) low level data has not been available, as well as being out of the scope.

6.3 System potentials with enhanced probability of detection

The HBR range extension concept is described by Willis [26]. The range extension possibilities of the HBR is apparent in the receiver centered oval of Cassini that describes the HBR coverage area. To extend the range, an improved S/N compared with the host must bee achieved within in the receiver site area. Comparing the bistatic and monostatic radar equations, given in equations 8 and 9, and assuming equal system losses leads to this requirement

$$(S/N)_B > (S/N)_M \Rightarrow \frac{\sigma_B G_R F_R^2}{{R_R}^2} > \frac{\sigma_M G_T {F_T}^2}{{R_T}^2} \tag{60}$$

While the gain of the transmitter is larger then the gain of the receiver ($G_R >> G_T$), this must be accommodated by short range from receiver to target ($R_R^2 << R_T^2$). With the experimental HBR, the gain of the receiving antenna was G_R=15dB while the transmitting antenna is G_T=40dB. Considering a requirement of the improved coverage area around the receiver site to be at range of at least 20km towards the host ($R_R \geq 20km$). Assuming bistatic LOS to targets and same RCS ($\sigma_B = \sigma_M$). To function as a range extension with this requirement, the receiver must operate at a baseline distance of about 230km. At this distance from T_X, low-level targets would be constraind by trasmitter LOS.
To illustrate a scenario, we have increase the reciever antenna gain to 30dB. This would equal to a 3.5m diameter parabolic dish at a frequency of 1.3GHz (using the approximation in equation 32). Increasing the size of the antenna will reduce the beamwidth (see equation 31), thereby increasing the localization accury. However, high directional antenna must resolve scan-on-scan issues. The HBR concept for high-end performance is relying on an advanced antenna doing digital beamforming in order to achieve such performance indicated here. Studies of the antenna is not within the scope of this work, but we have to som extent mimicked the performance of a moderately performing digital beamforming antenna by using a target directed reflector antenna slaved by the ADS-B signal.

With low signature-targets, the coverage area of the host is greatly reduced, and a HBR receiver can extend the coverage area of host whilst

staying well within transmitters radar horizon. Figure 46 illustrates the combined coverage area for low-signature targets (RCS=$0.01m^2$), using parameters from the experimental HBR, with the expetion of the increased antenna gain ($G_R = 30$dB). The detection threshold is set to 13dB for both transmitter and receiver and is marked with dark red color. We see the buldge around R_X provides coverage outside the coverage area of the host. In figure 47 we have taken the unlikely liberaty to move the transmitter position in order to illustrate, on the same map, how the receiver centered coverage area can be extened fully outside the hosts range. We see the bistatic oval of cassini around the receiver and the monostatic circle around the host.

To end the discussion, we would like to point in the direction of multiple low cost bistatic receiver systems. The straightforward soultion would be to have them non-overlapping, and thus the theory and results in this work could be applied directly together with the radar in the scene.

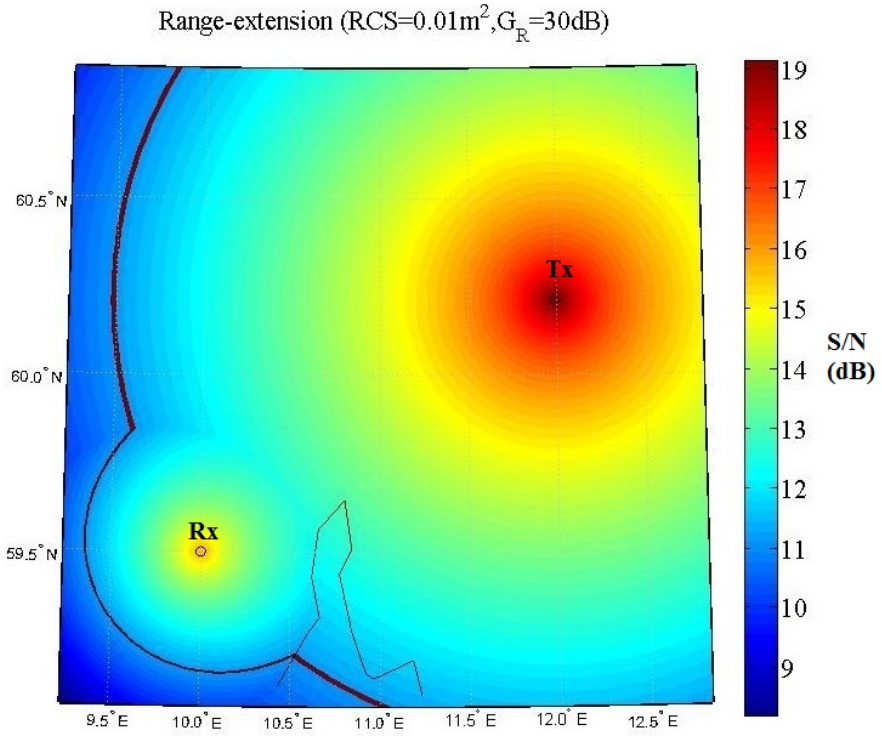

Figure 46: Combined coverage area for low signature targets (RCS=$0.01m^2$) within bistatic LOS (adapted from prosjekt).

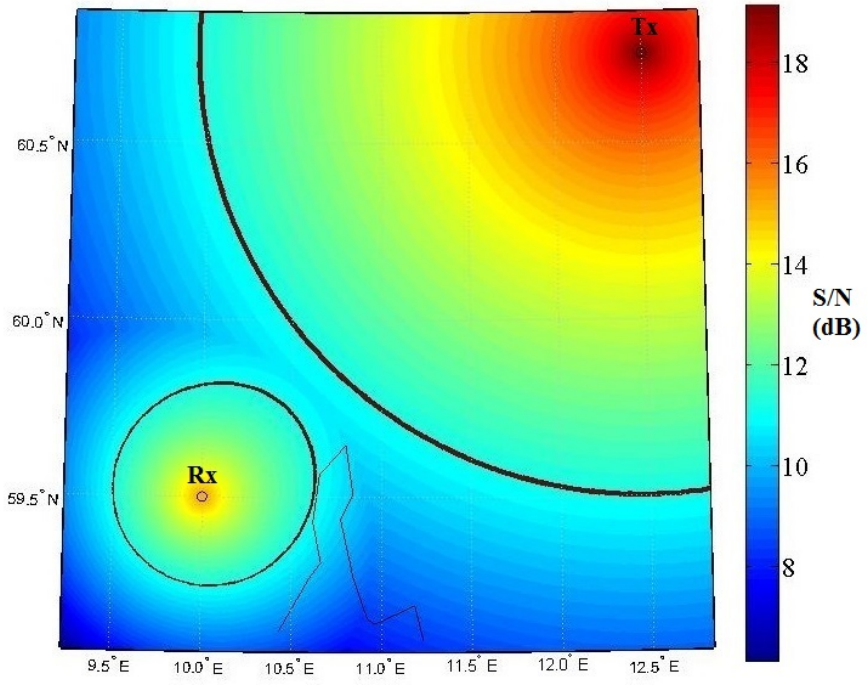

Figure 47: Transmitter(!) position moved to illustrate range extension completely outside the host's coverage area.

7 Summary and Conclusions

The only operational HBR that is referenced in open literature goes as far back in history as World War Two with the German Klein Heidelberg. However, if any operational HBR should exist, it is unlikely to be publicized due to the covert nature and military applications. The only successful military application of bistatic radar is the semi-active homing missile system concept, while it might be argued that the PCL-technology is also being promising.

HBR is a bistatic radar consisting of a passive receiver hitchhiking on an active radar. The advantages of bistatic radar stems from the separation of the transmitter and receiver which also introduces complexity in synchronization and target location.

An experimental HBR receiver has been developed in collaboration with FFI. Link budgets and measurements of the front-end components where made to estimate the detection capabilities. The receiving antenna is mounted on a pan/tilt pedestal directed to point at targets of opportunity to achieve maximum target dwell time, thus mimicking an electronically scanned antenna. Real data was recorded for analysis and post-processing.

Using real life data, methods for estimation of radar waveform parameters, PRF and scan-time for improved synchronization and localization of targets is demonstrated in chapter 4. PRF synchronized Time-Range matrix is used to display raw data along with ADS-B data converted to bistatic range to verify target detections. A large aircraft was detected 100km from the receiver site and an estimated range of 180km for similar targets is proposed.

Pulse compression, non-coherent integration and coherent range-Doppler integration were applied on real life data. Target detections were plotted on a Cartesian grid by solving the geometry for the bistatic triangle

LOS constrains and required S/N for target detections, excludes the HBR to be applicable in all situations. However, in areas where the terrain and proximity to other sensors allows for HBR operations, the HBR can serve as a complementary sensor for air surveillance.

If synchronization with the host is achieved, the targets within LOS of both T_X and R_X could be detected and localized. This would augment the probability of detecting low signature targets within the common coverage area and extend the total coverage into areas not fully covered by the host radar. In situations where the synchronization with T_X may not be adequate for localization, a HBR could still provide with target detections.

The HBR concept is promising and could provide coverage in areas of interest from a military perspective. The bistatic receiver could in certain situations improve target detection as indicated in chapter 6, "Future Perspectives and System Potential". In particular modern radars, offering high flexibilty, beam steering and waveform design, could serve as a viable cooperative transmitter.

Future work that may be considered is; further hardware development to reduce system noise temperature, thus improving the probability of detection, implementations of real time processing and digital PPI localization of targets, in-direct synchronization with GPS-time with a cooperative host and simulations or experiments in particular geographical areas of military interest.

This project has demonstrated:

- Experimental HBR receiver hardware setup which enables collection of real life data for analysis and parameter estimation
- The digital signal processing techniques which were evaluated includes: raw data display, pulse compression, non-coherent integration, and finally coherent range-Doppler processing. The latter was made possible after analysis of the received waveform from the transmitter. In particular, the phase of the stationary clutter return were estimated, and corrected for, in which the moving targets in the scene were properly distinguished from clutter.
- Simulations and considerations for future HBR operations were also considered, and numerical examples in order to illustrate concepts were presented.

References

[1] Ieee standard radar definitions. *IEEE Std 686-1997*, 1998.

[2] Clive Alabaster. *Pulse Doppler Radar: Principles, Technology, Applications*. Scitech Publishing, 2012.

[3] H.D. Baker, C.J. Griffiths. Bistatic and multistatic radar sensors for homeland security. In *Conference of the NATO Advanced-Study-Institute on Advances in Sensing with Security Applications*, 2005.

[4] D. I. Crecraft, S. Gergely. *Analog Electronics: Circuits, Systems and Signal Processing*. Butterworth Heinemann, 2002.

[5] A. Elias-Fuste, R. De Porrata-Doria, A. Broquetas, A. Aguasca, and J. F. Muniain. "brenda" bistatic radar equipment data acquisition (a barcelona bistatic radar experiment). In *Microwave Conference, 1993. 23rd European*, pages 475–477, 1993.

[6] H. Griffiths and N. Willis. Klein heidelberg 151;the first modern bistatic radar system. *Aerospace and Electronic Systems, IEEE Transactions on*, 46(4):1571–1588, 2010.

[7] H. D. Griffiths. From a different perspective: Principles, practice and potential of bistatic radar. *IEE 2003, Radar 2003*, 2003.

[8] Bert C. Henderson. Mixers in microwave systems: Part 1. 17(1), January 1990.

[9] Sindre Strømøy Idar Norheim-Næss, Børge Torvik. Ffi-notat 2012/02194 esm antenne decs 608101 - gjenbruk, gjenoppsett og målføging med ads-b for bistatisk radar og innsamling av målsignaturer. 2012.

[10] National Instruments. Convolution and polynomial multiplication. `http://zone.ni.com/devzone/cda/p/id/6525`. Accessed: 2013-05-06.

[11] M.C. Jackson. The geometry of bistatic radar systems. *Communications, Radar and Signal Processing, IEE Proceedings F*, 133(7):604–612, 1986.

[12] T. Johnsen and K.E. Olsen. Hitchhiking bistatic radar: principles, processing and experimental findings. In *Radar Conference, 2007 IEEE*, pages 518–523, 2007.

[13] Nadav Levanon. *Radar Principles*. 1988.

[14] Bassem R. Mahafza. *Radar Systems Analysis and Design Using MATLAB*. CRC Press LLC, 2000.

[15] William A. Holm Mark A. Richards, James A. Scheer. *Principles of Modern Radar: Basic Principles.* SciTech Publishing Inc, 2010.

[16] M. Mazur, M. Sankowski, T. Nowak, A. Nalewaja, and J. Pedziwiatr. Capabilities of a bistatic receivers' network using hyperbolic positioning method. In *Microwave Radar and Wireless Communications (MIKON), 2012 19th International Conference on*, volume 1, pages 357–360, 2012.

[17] K. E. Olsen. *Investigation of bandwidth utilisation methods to optimise performance in passive bistatic radar.* PhD thesis, UCL (University College London), 2011.

[18] Sophocles J. Orfanidis. *Electromagnetic Waves and Antennas.* www.ece.rutgers.edu/ orfanidi/ewa, 2012.

[19] O. Overrein, K.E. Olsen, S. Johnsrud, P.K. Sornes, T. Johnsen, J. Navarro, V. Sahajpal, and R.O. Stemland. Geometrical and signal processing aspects using a bistatic hitchhiking radar system. In *Radar Conference, 2005 IEEE International*, pages 332–336, 2005.

[20] J. G. Schoenenberger and J.R. Forrest. Principles of independent receivers for use with co-operative radar transmitters. *Radio and Electronic Engineer*, 52(2):93–, 1982.

[21] Alejandro Aragon-Zavala Simon Saunders. *Antennas and Propagation for Wireless Communication Systems: 2nd Edition.* JohnWiley Sons Ltd, 2007.

[22] Merrill I. Skolnik. *Radar Handbook, Third Edition.* "McGraw Hill", 2008.

[23] Sindre Strømøy. Prosjektoppgave i unik4680 - deteksjon av fly med en passiv bistatisk radarmottaker, haikende på en primærradar. Descember 2012.

[24] Karl Erik Olsen Terje Johnsen. Bi- and multistatic radar. *NATO RTO-EN-SET-86*, 2006.

[25] T. Tsao, M. Slamani, P. Varshney, D. Weiner, H. Schwarzlander, and S. Borek. Ambiguity function for a bistatic radar. *Aerospace and Electronic Systems, IEEE Transactions on*, 33(3):1041–1051, 1997.

[26] Nicholas J. Willis. *Bistatic Radar, 2nd Edition.* 1995.

[27] Nicholas J. Willis and Hugh D. Griffiths. *Advances in Bistatic Radar.* 2007.

Appendix

A Hardware Descriptions

A.1 Antenna

Q-PAR QSR 700-OST
RF=1300MHz
Gain: 15dBi
-3dB beamwidth: 23deg
-10dB beamwidth: 45deg
recommended far-field: >59m

Online datasheet:
`https://www.q-par.com/products/reflector-antennas/0-9-18-ghz-dual-polarised-horn-in-a-0-7m-reflector/files/wbhdp900mhz-18sfeed-with-qsr700-ost-reflector_web.pdf`
[05.16.2013]

A.2 LNA

Mini-Circuits ZX60-1614LN
Gain: 15dB
NF: 0.5dB
P1dB: 13.5dBm
Pin DC: 15V

Online datasheet:
`http://217.34.103.131/pdfs/ZX60-1614LN.pdf` [05.16.2013]

A.3 RF-BP

Center freq. : 1300MHz
-3dB Pass band : ca.100MHz
-70dB Pass band: ca.200MHz I.L (1.3GHz): max 1.3dB
No datasheet
Own measurements:

Figure 48: RF-BP 1200-1400MHz

A.4 Mixer

Mini-Circuits ZFM-150
RF=1300MHz
C.L: 6.7dB
LO Power: +10dB
LO-RF isolation: 35dB
LO-IF isolation: 30dB
Online datasheet:
`http://217.34.103.131/pdfs/ZFM-150.pdf` [05.16.2013]

A.5 IF-BP

Mini-Circuits SBP-70+
50Ω Elliptic Response
Center freq. : 70MHz
-1.5dB Pass band: ca.14MHz
-3dB Pass band : ca.24MHz
-35dB band : 6-193MHZ
I.L (70MHz) : max 1.5dB
VSWR (Pass band): max1.7:1

max input : 0.5W

Online datasheet:
http://www.minicircuits.com/pdfs/SBP-70+.pdf [05.16.2013]

A.6 IF-AMP

Miteq AU-1310
IF: 70MHz
Gain: 33dB
NF: 1.4dB
P1dB: +9dBm
Pin(DC): 15V

Online datasheet:
http://www.miteq.com/docs/1310.PDF[05.16.2013]

B Spreadsheets

B.1 Noise Figure Calculator

Pi was generated with 1.3GHz CW
A 3dB Attenuater was used to simulate 4m cableloss

Pi(dBm)	Po(dBm)	G(dB)	No(-dBm)	So/No	NF(dB)	Ts(K)
-35	0,8	35,8	-78	78,8	5,428787	722,2243
-40	-4,2	35,8	-78	73,8	5,428787	722,2243
-45	-11,5	33,5	-78	66,5	7,728787	1429,003
-50	-16,6	33,4	-78	61,4	7,828787	1469,044
-55	-21,5	33,5	-78	56,5	7,728787	1429,003
-60	-26,3	33,7	-78	51,7	7,528787	1351,636
-65	-31,3	33,7	-78	46,7	7,528787	1351,636
-70	-36,3	33,7	-78	41,7	7,528787	1351,636
-75	-41,4	33,6	-78	36,6	7,628787	1389,874
-80	-46,5	33,5	-78	31,5	7,728787	1429,003
-85	-51,6	33,4	-78	26,4	7,828787	1469,044
-90	-56,4	33,6	-78	21,6	7,628787	1389,874
-95	-61,5	33,5	-78	16,5	7,728787	1429,003
-100	-66,4	33,6	-78	11,6	7,628787	1389,874
-105	-70,7	34,3	-78	7,3	6,928787	1139,805
-110	-74,2	35,8	-78	3,8	5,428787	722,2243
-115	-76,7	38,3	-78	1,3	2,928787	279,2155

No(dBm)	-78	NF(dB)	7,52878745
G(dB)	33,7	Ts(K)	1351,63553
RBW	300000		

NF=No-G-Ni+1,7dB

Gain of signals less than -100dBm is affected by the noisefloor

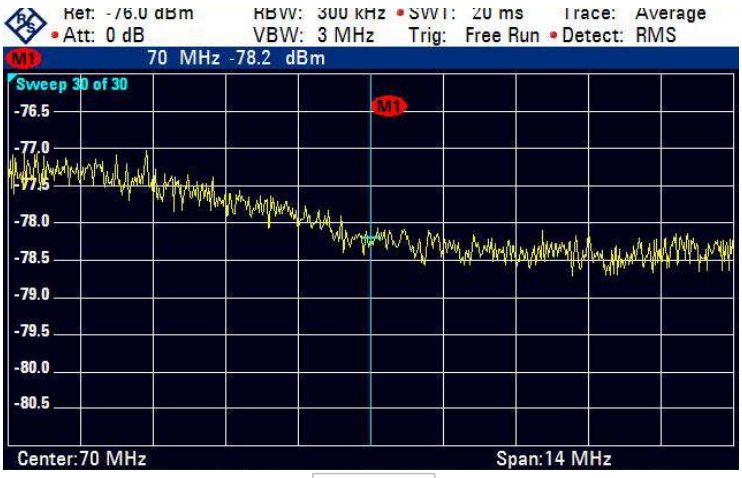

Noise Floor

B.2 Bistatic Equation Parameters

Bistatic Radar Equation

$$S/N = \frac{P_T G_T G_R \lambda^2 \sigma_B F_T^2 F_R^2}{(4\pi)^3 R_T^2 R_R^2 k T_s B_n L_T L_R} \qquad P_R = \frac{P_T G_T G_R \lambda^2 \sigma_B F_T^2 F_R^2}{(4\pi)^3 R_T^2 R_R^2 L_T}$$

Inputs		
Pt	2	MW
Gt	40	dB
Gr	15	dB
sigma	50	m^2
fc	1,3	GHz
Ft^2	0	dB
Fr^2	0	dB
Rt	180	km
Rr	180	km
Bn	2,2	MHz
Lt	3	dB
Lr	5	dB
PCG	10	dB

	Linear		Logarithmic	
Pt	2000000	W	63,01029996	dBW
Gt	10000		40	
Gr	31,6227766		15	
sigma_b	50		16,98970004	
lamda^2	0,053254438		-12,736442	
Ft^2	1		0	
Fr^2	1		0	
PCG	10		10	
(4*pi)^3	1984,401708		32,97629592	
Rt^2	32400000000		105,1054501	
Rr^2	32400000000		105,1054501	
Bn	2200000		63,42422681	
Lt	1,995262315		3	
Lr	3,16227766		5	
k	1,38E-23		-228,601209	
Ts	1351,635531		31,308596	

	Linear (W)	dBW	Linear (mW)	dBm
Pr	4,05169E-13	-123,9236	4,05169E-10	-93,9236
S/N	31,22301412	14,94475		

S/N include Pulse Compression Gain

	dBm	V(50ohm)	mV	mVpeak
ADC Pin	-60,2036381	0,000218	0,218425379	0,308853

Max Vpeak of ADC = 0.95Vpeak

Power of ADC input (Pr*Overall gain of receiver)

	Linear	dB	dBm	mV
Noise out	9,6641E-10	-90,14839	-60,1483863	0,219819

No=kTsB*receiver gain

Noise in	4,554E-15	-143,4161	-113,41607	0,000477

Ni=kTaB

Receiver Noise Figure Cascade Calculator

(Inspired by http://www.microwaves101.com/encyclopedia/noisefigure.cfm)

	Inputs	Outputs										
Antenna Noise Temperature	Antenna	Coax cable										
Gain(dB)		-3										
T (K)	150	290										
T(ant+cable)	219,8337873	***T_(ant+cable)=T_ant*G_cable(linear)+T_cable*(1-G_cable(linear))***										
Chain:	0	1	2	3	4	5	6	7	8	9	10	
Components:	Antenna w/cable	RF BP filter	cable	LNA	mixer	IF BP filter	IF amp	IF BP filter				
Component data												
Gain(dB)	-3	-1,5	-0,5	14,82	-6,7	-1,2	33	-1,2				
NF(dB)	2,450306154	1,5	0,5	0,5	6,7	1,2	1,2	1,2				
Calculated linear data [=10^(dB/10)]												
Gain(linear)	0,501187234	0,707946	0,891251	30,33891	0,213796	0,758578	1995,262	0,758578	1	1	1	
F(linear)	1,758047542	1,412538	1,122018	1,122018	4,677351	1,318257	1,318257	1,318257	1	1	1	
Cascaded linear values(Noise Factor (F) is caclulated with Friis Formula)												
Gain(linear)	0,501187234	0,354813	0,316228	9,594006	2,051162	1,555966	3104,56	2355,049	2355,049	2355,049	2355,049	
F(linear)	1,758047542	3,170585	3,51448	3,900336	4,283633	4,438792	4,643332	4,643434	4,643434	4,643434	4,643434	
T(K)	219,8337873	629,4697	729,1991	841,0975	952,2535	997,2497	1056,566	1056,596	1056,596	1056,596	1056,596	
Cascaded dB values												
Gain(dB)		-4,5	-5	9,82	3,12	1,92	34,92	33,72	33,72	33,72	33,72	
NF(dB)	2,450306154	5,011394	5,458611	5,91102	6,318122	6,472648	6,668297	6,668393	6,668393	6,668393	6,668393	
Comments:	estimated	measured	measured	datasheet	datasheet	datasheet	datasheet	datasheet				
				Mini-Circuits	Mini-Circuits	Mini-Circuits	Miteq	Mini-Circuits				
Type				ZX60-1614LN	ZFM-150	SBP-70	AU-1310	SBP-70				
Frequency				1,3 GHz	1,3 GHz	70 MHz	70 MHz	70 MHz				
P1dBm out				13.5 dBm	LO=10dBm		9 dBm					

B.4 Target Track

Time	BR(m)	S(dBm)	S/N(dB)
11,8	24425,82	-18,3	34,7
23,5	27655,73	-12,5	40,5
35,2	31410,73	-15,3	37,7
46,9	35106,17	-11	42
58,6	39687,96	-12,1	40,9
70,3	44049,46	-19,3	33,7
82	48554,95	-23,6	29,4
93,8	52834,7	-10,4	42,6
105,5	57616,56	-23	30
117,2	62781,94	-23,4	29,6
129	67767,56	-14	39
140,7	72133,12	-18,4	34,6
152,4	77118,86	-21,4	31,6
164,1	82312,09	-21,9	31,1
175,8	86937,2	-26,5	26,5
187,5	92110,23	-21,6	31,4
199,3	97578,7	-23,7	29,3
211	102720,4	-22,6	30,4
222,7	107803,6	-21,1	31,9
234,5	113089	-20,5	32,5
246,2	118225,8	-26,3	26,7
258	123473,5	-29,1	23,9
269,7	128565,7	-25,2	27,8
281,4	133768,6	-23,9	29,1
293,2	139160,7	-24,7	28,3
304,9	144122,7	-19	34
316,6	149629,8	-20,9	32,1
328,4	155155,9	-22,6	30,4
340,1	160505,2	-29,1	23,9
351,9	165598	-30,6	22,4
363,6	170875,4	-29,2	23,8
375,3	176449,7	-33,5	19,5
387,1	184847,5	-29,6	23,4
398,8	186950	-30,5	22,5
410,6	192613,7	-27,4	25,6
422,3	198009,1	-28,5	24,5
434	203411,5	-27,7	25,3

C PT-3002 Pelco-D Steering

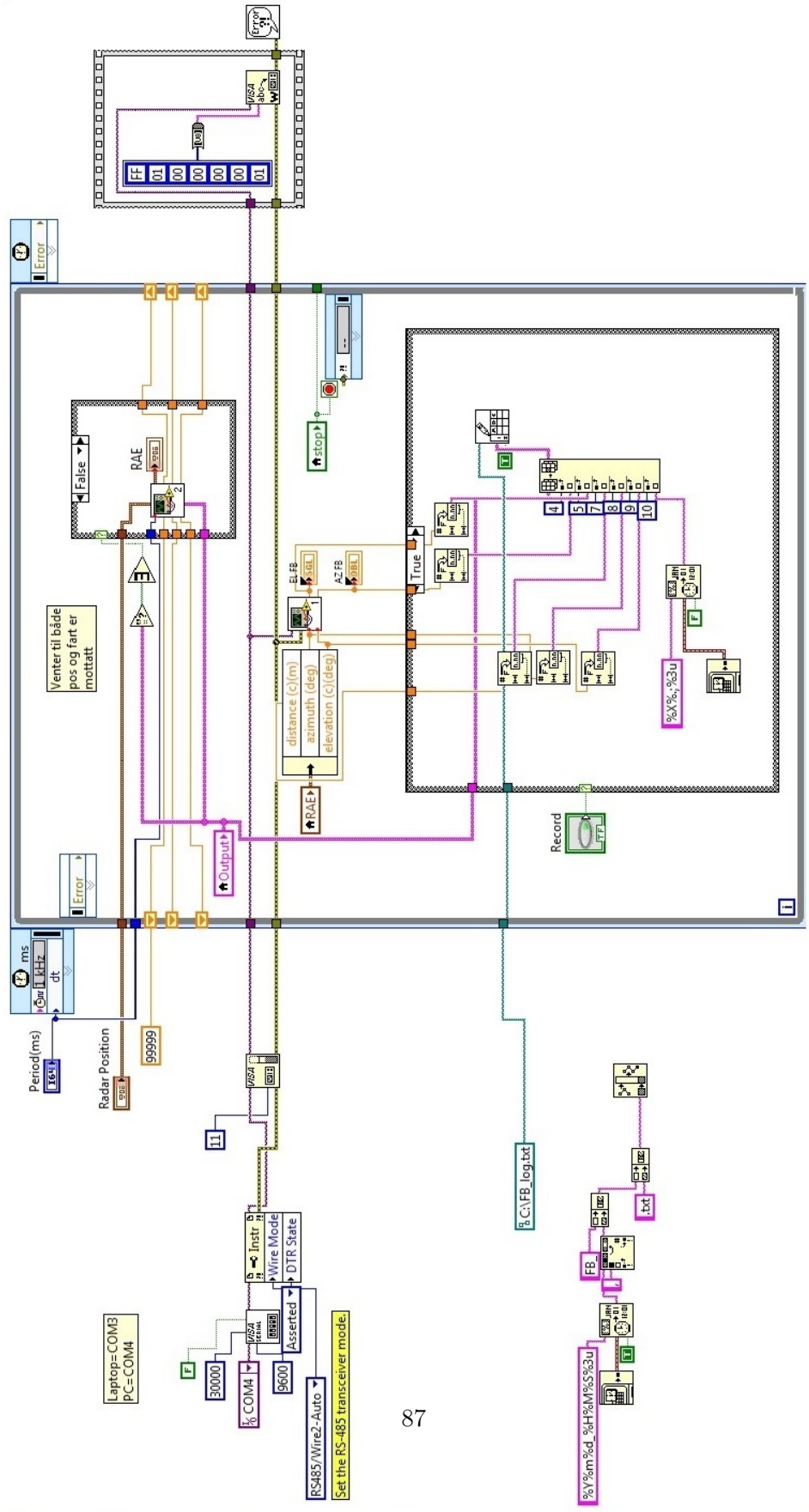
Error
FF 01 00 00 00 00 01
Error
False
RAE
Venter til både pos og fart er mottatt
stop
EL FB
AZ FB
distance (c)(m)
azimuth (deg)
elevation (c)(deg)
RAE
Output
True
%X%,%3u
Record
Error
ms
dt
Period(ms)
Radar Position
99999
11
Instr
Wire Mode
DTR State
Laptop=COM3
PC=COM4
30000
COM4
9600
Asserted
RS485/Wire2-Auto
Set the RS-485 transceiver mode.
C:\FB_log.txt
.txt
FB
%Y%m%d_%H%M%S%3u

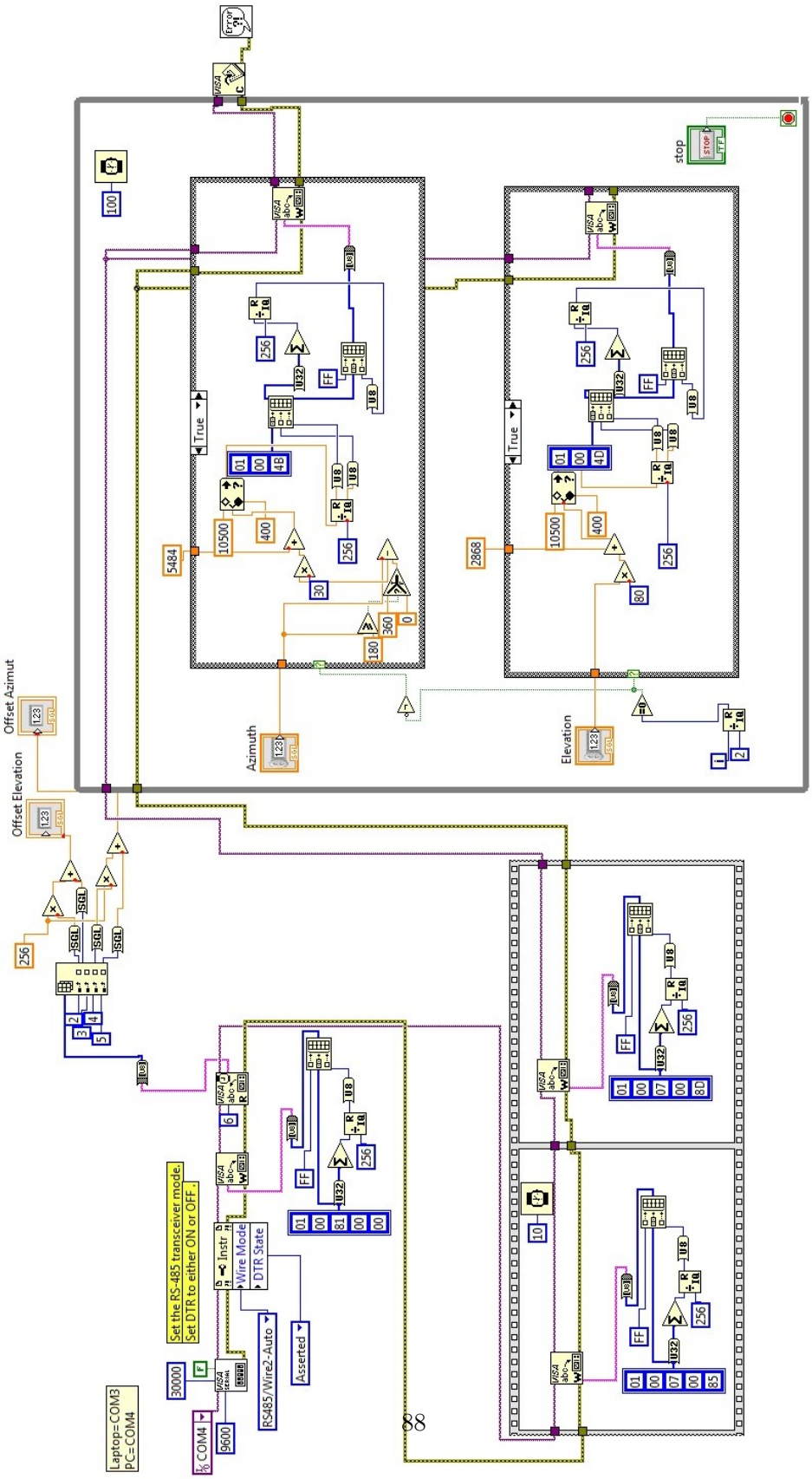
Offset Azimut
Offset Elevation
Azimuth
Elevation
stop
Set the RS-485 transceiver mode.
Set DTR to either ON or OFF.
Laptop=COM3
PC=COM4
RS485/Wire2-Auto
Asserted
COM4
9600
30000

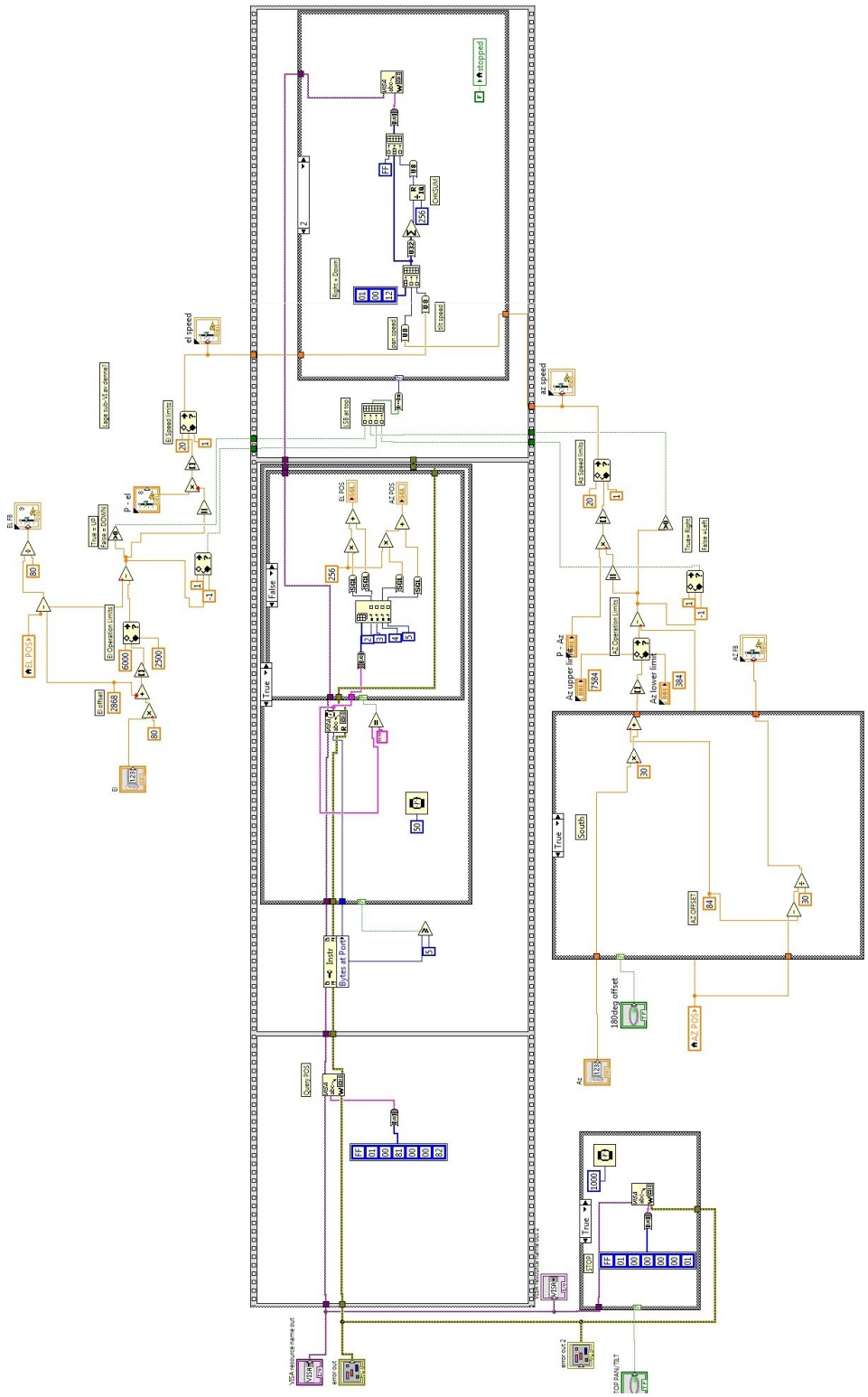
stopped
el speed
az speed
El Speed limits
Az Speed limits
El Operation limits
Az Operation limits
El offset
Az upper limit
Az lower limit
180deg offset
AZ OFFSET
South
Right + Down
Left + Up
Bytes at Port
Open VISA
VISA resource name out
error out
error out 2
TCP PAN/TILT

D Matlab Codes

```
%%%%%%%%%%%%%%%%%%%%%%%%%%%%%
% HBR
%%%%%%%%%%%%%%%%%%%%%%%%%%%%%
clear all
%close all
Fs = (100/23)*1e6; % Sampling frequency
T = 1/Fs; % Sample time
pri=13392+0.2517-0.00471; %KV is +0.2517 %484561 KV-0.0047
S = ceil(0*Fs);
npri=ceil((S/pri))-1;
S=1+round(npri*pri*1); %Starttime

k=(sqrt(2)*(1.9/2))/(2^21);%convert to Vrms
fid = fopen('Hiker_20130405_114357620.dat','r','ieee-be'); % Open the binary file
fseek(fid,S*8,'bof');

L = ceil(20*Fs);% Length of signal in sec

Data = fread(fid,2*L,'int32',0,'ieee-be')*k;
z= Data(1:2:end) + 1i*Data(2:2:end);
L=size(z,1);
max(abs(z))
10*log10(20*((max(abs(z)))^2))
%%
%pulsecompression
cl=2;%chiplength of Barker-13
%timeinverted matched filter
mf=[ones(1,5*cl),-ones(1,2*cl),ones(1,2*cl),-ones(1,cl),ones(1,cl),-ones(1,cl),ones(1,↙
cl)];
z=conv(mf,z);
%%
a=0;
pri=13392+0.2517-0.00471-0.00157; %KV is +0.2517 %484561 KV-0.0047
npri=ceil((size(z,1)/pri))-1;
rm=zeros(npri,3500);
%z=(z(106:end));

    ll=1+round(npri*pri*(1-1));
    ul=1+round(npri*pri*1);
    z=z(ll:ul);

    for k=1:npri
        mll=1+round((k-1)*pri);
        mul=1+round(k*pri);
        bin=z(mll:mul);
        rm(k,:)=abs(bin(1681:5180));
    end
  %%
    figure
    y=npri*pri/Fs;
    x=(3e8/Fs)*3500;%pri;
   imagesc([0 x],[0 y],10*log10(20*rm.^2),[-50 -25])
   % imagesc(10*log10(20*rm.^2),[-57 -5])
    xlabel('relative range(m)')
    ylabel('time (s)')
```

```
    title('484561')
    colorbar

% Plot ADS-B

    cc=hsv(12);
hold on
for k=1:length(ADSB)
    range=ADSB{k};
    plot(range(:,2),range(:,1),'x','color',cc(k,:))
    axis([0 69000 0 80])
    set(gca,'YDir','reverse');
end
```

```
%%%%%%%%%%%%%%%%%%%%%%%%%%%%%%%%%%%%%%%%%%%%%%%%%%%%
% Noise Measurements after pulse compression
%%%%%%%%%%%%%%%%%%%%%%%%%%%%%%%%%%%%%%%%%%%%%%%%%%%%
load('close_target.mat')
%%
np=16;
N=floor(size(rm,1)/np);
ci=zeros(N,size(rm,2));
nci=zeros(N,size(rm,2));
for k=1:N
ci(k,:)=sum(rm(1+np*(k-1):np*k,:))./np;
nci(k,:)=sum(abs(rm(1+np*(k-1):np*k,:)))./np;
end
%%
patch1= rm(2001:2200,801:1000); %noise
patch2=ci(151:350,801:1000);
patch3=nci(151:350,801:1000);

figure;
subplot(3,1,1),hist(1000*abs(patch1(:)), size(patch1,1));
title('Noise Measure - Amplitude distribution')
xlabel('No integration. mV_{rms} (0.5mV = -53dBm)')

subplot(3,1,2),hist(1000*abs(patch2(:)), size(patch1,1));
xlabel('Coherent integration. mV_{rms} (0.12mV = -65dBm)')

subplot(3,1,3),hist(1000*abs(patch3(:)), size(patch1,1));
xlabel('Non-coherent integration. mV_{rms} (0.5mV = -53dBm)')
%%
%Pulse integration
%rm=rm(201:1200,1:800);
rm=rm(4567-499:4567+500,1:800);

np=16;
N=floor(size(rm,1)/np);
nci=zeros(N,size(rm,2));
for k=1:N
nci(k,:)=sum(abs(rm(1+(np*(k-1)):np*k,:)))./np;
end
%%
figure
imagesc(10*log10(20*abs(rm).^2)+53,[0 40]);
colorbar
title('no integration')
figure
imagesc(10*log10(20*abs(nci).^2)+53,[0 40]);
colorbar
title('non-coherent sum')
%%
figure
subplot(2,1,2),plot((1:800)*0.069,10*log10(20*abs(nci(48,:)).^2)+53)
axis([0 5.5 -15 35])
title('Non-coherent integration')
ylabel('S/N(dB)')
subplot(2,1,1),plot((1:800)*0.069,10*log10(20*abs(rm(480,:)).^2)+53)
```

```
axis([0 5.5 -15 35])
title('No pulse integration')
```

```
%%%%%%%%%%%%%%%%%%%%%%%%%%%%%%%
%Target Location
%%%%%%%%%%%%%%%%%%%%%%%%%%%%%%%

% Change default axes fonts.
set(0,'DefaultAxesFontName', 'Times New Roman')
set(0,'DefaultAxesFontSize', 16)

% Change default text fonts.
set(0,'DefaultTextFontname', 'Times New Roman')
set(0,'DefaultTextFontSize', 16)

%Position of Tx and Rx
FFI=load('FFI.mat');
KV=load('KV.mat')

load('close_target') %time-range matrix
rm=rm(1980:5800,:);
x=size(rm,2);
imagesc([0 x*0.0069],[0 360],10*log10(20*abs(rm).^2),[-53 -5])
%non-coherent pulse compression
np=16;
N=floor(size(rm,1)/np);
for k=1:N
snci(k,:)=sum(abs(rm(1+np*(k-1):np*k,:)))./np;
end
%%

Fs = (100/23)*1e6; % Sampling frequency
pri=13392+0.2517-0.00471-0.00015;
npri=ceil((size(snci,1)/pri))-1;
L_True=lla2dist(KV,FFI);
L=ceil(L_True/(3e8/Fs));


%%
figure
    y=npri*pri/Fs;
    x=(3e8/Fs)*1850;%pri;
  imagesc([0 x],[80 y+80],10*log10(20*abs(snci).^2),[-53 -5])

%%
%map=imread('kart.jpg'); %Show on map
%imagesc([10 -100],[10 -100],map)
%axis xy
%axis equal
%hold on
plot(0,0,'or','MarkerSize',10)
xlabel('km')
ylabel('km')
axis([-103 17 -73 12])
%axis equal
hold on
y=58.65*cos(deg2rad(243));
x=58.65*sin(deg2rad(243));
```

```
plot(x,y,'or','MarkerSize',10)
%%
thetha_T=-asin(cos(deg2rad(linspace(0,360-(360/size(snci,1)),size(snci,1))-azimuth(FFI↙
(1:2)',KV(1:2)'))));

Az=deg2rad(linspace(0,360-(360/size(snci,1)),size(snci,1)));

for i=1:size(thetha_T,2)
    for j=1:size(snci,2)-1
        if (10*log10(20*abs(snci(i,j)).^2)) > -38
            R_T=0.001*(3e8/Fs)*(((j+L)^2-L^2)/(2*((j+L)-L*sin(thetha_T(i)))));
            %R_T=((j+L)^2+2*L)/(2*(j+L)+1-sin(thetha_T(i)));
            %R_T=0.001*(3e8/Fs)*(R_T-(L/2));
            y=R_T*cos(Az(i));
            x=R_T*sin(Az(i));
            %polar(Az(i),R_T,'x')
            if(10*log10(20*abs(snci(i,j)).^2)) > -20
            plot(x,y,'x','MarkerSize',5);
            else
            plot(x,y)
            end
            %pause(0.1) %simulate plots by time
        end
    end
end
```